# A Setting-Less and Boundary-Element-Independent Directional Pilot Protection for Multiterminal HVDC Systems

Jiawei He, *Member, IEEE*, Mingyu Shao, Bohao Zhou, Zhongrun Xie, Ye Li, Jun Li, and Bin Li, *Senior Member, IEEE*

***Abstract*—The application scenarios of high-voltage direct current systems are becoming increasingly diverse, featuring complex and variable topologies as well as boundary conditions. Existing single-ended protection methods for dc lines cannot ensure selectivity of operation in the absence of line boundaries. The pilot protection can identify faults without relying on line boundaries, but it generally depends heavily on precise system parameters or requires a cumbersome threshold value selection process. This study analyzes the transient impedance phase-frequency characteristics of dc systems after faults under three typical scenarios, i.e., no boundary, dc reactor boundary, and dc filter boundary. Based on the polarity characteristic of high-frequency transient power during forward and backward faults, a novel directional pilot protection for dc lines is proposed. Compared to existing methods, this approach does not depend on system parameters or boundary elements, and eliminates the need for threshold setting, significantly reducing the complexity of engineering implementation and maintenance. Finally, a prototype of the fast directional pilot protection device is developed based on the proposed method, and extensive hardware-in-loop testing is conducted on the real time digital simulator platform to validate its operation performance.**

***Index Terms*—Directional pilot protection, high-voltage direct current (HVDC) systems, line boundary, setting-less.**

## I. Introduction

As the demand for large-scale renewable power transmission over long distances has increased, the advantages of high-voltage direct current (HVDC) systems, such as low transmission losses, high transmission capacity, and compact power corridors, have become increasingly apparent. However, the limited overcurrent ability of power electronic devices in HVDC systems, particularly the modular multilevel converter (MMC) based HVDC systems, imposes higher requirements for protection techniques [1]. Currently, the dc line protection mainly includes single-ended and pilot protections, with the former typically serving as the main protection and the latter as backup protection. With the development of dc transmission technology, the application scenarios of dc systems are becoming more complex, e.g., long-distance power transmission on land, asynchronous grids interconnection, and offshore wind power transmission [2], [3]. In the above scenarios, the topology of the dc system, types of converter stations, and configuration of components such as filters and current limiters vary significantly, presenting new challenges for the sensitivity and reliability of dc line protections.

The single-ended protection based on change or rate of change of electrical quantities, such as voltage and current traveling wave (TW), is widely used in line-commutated converter based HVDC (LCC-HVDC) systems [4]. However, existing research indicates that, the typical single-ended TW based protections have weak ability against high transition resistance. To improve the ability against transition resistance, Zhang et al. [5] utilized 0-mode fitted parameters to reflect fault distance and impedance, then adaptively adjusted the threshold value of rate of change of voltage protection, thereby enhancing tolerance to transition resistance. Zhang et al. [6] used a zero-mode fault current at the midpoint of the line as a reference, and constructed criteria for identifying internal and external faults using the Pearson correlation coefficient. It can improve the ability against transition resistance, however, is not suitable for bipolar faults. In MMC-HVDC systems, the existence of the current-limiting reactor creates more beneficial features for protection against transition resistance. Consequently, researchers have used wavelet transform to extract high-frequency transient information to design protections [7]. In addition, Zhang et al. [8] introduced a model recognition method using the Levenberg-Marquardt optimization algorithm to identify fault modes from measured fault voltages and distinguish fault segments, offering notable advantages, such as eliminating the need for threshold setting.

Received 4 February 2025; revised 17 April 2025 and 25 June 2025; accepted 7 August 2025. Date of publication 15 August 2025; date of current version 22 October 2025. This work was supported in part by the National Natural Science Foundation of China under Grant 52207129, in part by the National Natural Science Foundation of China for Distinguished Young Scholars under Grant 52025071, and in part by the National Natural Science Foundation of China under Grant 52207088. Recommended for publication by Associate Editor X. Pei. *(Corresponding authors: Bohao Zhou; Bin Li.)*

Jiawei He, Mingyu Shao, and Bin Li are with the State key laboratory of Smart Power Distribution Equipment and System, Tianjin University, Tianjin 300072, China (e-mail: hejiawei_tju@126.com; binli@tju.edu.cn).

Bohao Zhou is with the National Industry-Education Platform for Energy Storage, Tianjin University, Tianjin 300350, China (e-mail: zhoubohao@tju.edu.cn).

Zhongrun Xie is with the Power Dispatching and Control Center of Guizhou Power Grid Company Ltd., Guiyang 550000, China.

Ye Li is with the State key laboratory of Smart Power Distribution Equipment and System, Hebei University of Technology, Tianjin 300132, China.

Jun Li is with the DC Technology Center of State Grid Corporation of China, Beijing 100053, China.

Color versions of one or more figures in this article are available at https://doi.org/10.1109/TPEL.2025.3599369.

Digital Object Identifier 10.1109/TPEL.2025.3599369

It should be noted that the aforementioned single-ended protections are all dependent on the boundary elements at both ends of the line, such as dc filters and dc reactors. As the scale and topology complexity of HVDC systems increase, these boundary elements may no longer be installed at the ends of lines. For example, in Kun-Liu-Long three-terminal HVDC system in China, because the used converters themselves have the fault current limiting and clearing capability [9], [10], there is no need to install current-limiting reactors at either end of the lines anymore (reactors were installed only at the outlets of the converter stations). In addition, in offshore wind power HVDC transmission systems, the volume and weight constraint on offshore platforms typically result in the absence of filters, current-limiting reactors, or other boundary elements at the line end. In such cases, single-ended protections based on boundary characteristics struggle to ensure selectivity and cannot achieve a full-line quick action.

Pilot protections typically utilize information from both ends of the line to achieve fault discrimination, such as current differential protection and directional pilot protection. In theory, it offers absolute selectivity and high sensitivity [11]. Therefore, the pilot protection can be considered as the primary protection for dc lines in multiterminal HVDC systems where boundary elements are absent. The existing current differential protection for dc lines directly utilizes the sampled current values from both ends to calculate the differential current. To avoid the unbalanced current caused by the transient charging and discharging of long-line distributed capacitors, a delay of several hundred milliseconds or more is typically required, resulting in an operating time of the order of seconds [12]. To address this issue, Tzelepis et al. [13] proposed to design differential protection criteria using currents measured from multiple points along the line, to reduce the influence of the distributed capacitance current. It can improve the operating speed of current differential protection to a certain extent but does not fundamentally resolve the issue of distributed capacitance currents. Gao et al. [14], and Liu et al. [15] introduced the Bergeron-model-based current differential protection principle, which automatically compensates for the distributed capacitance current, and thus significantly reduce the operation time.

The current differential protection requires transmitting analogue signals, which imposes high demands on communication and synchronization. In contrast, the directional pilot protection only needs to transmit digital directional signals without the need for data synchronization, significantly reducing the complexity of engineering implementation. Moreover, to simplify engineering implementation, most of manufacturers' dc protection hardware platforms currently do not allocate channels for signal synchronization. So the technical advantages of directional pilot protection are further highlighted. Kong et al. [16] utilize the energy of fault voltage TW to construct a directional criterion. Yu and Xiao [17], and Li et al. [18] extracted high-frequency transient to mitigate the adverse effect of line parameters frequency-dependent character on the TW-based directional pilot protection. Above directional pilot protections have excellent performance in HVDC systems, while the main drawback is the high dependence on system parameters (such as line wave impedance).

The aforementioned pilot protections, such as current differential protection and directional pilot protection, do not rely on line boundaries. However, the design of the protection criteria requires prior acquisition of accurate system parameters, and the threshold value setting process is complex. In different application scenarios and climatic conditions, accurately obtaining system parameters, especially those of the line, and making real-time adjustments to the thresholds can be challenging, undermining the reliability and robustness of protection. Therefore, for various HVDC transmission application scenarios, such as "sandy areas" and "deep offshore," further research is needed to develop new dc protection principle that is more universally applicable and easier to implement in engineering contexts.

To this end, this study proposes a novel directional pilot protection algorithm. The main innovation and technical advantages of this study are as follows.

1) The phase-frequency characteristics of transient impedance during forward and backward faults in dc systems with different boundary conditions were analyzed. It is then concluded that the maximum value polarity of high-frequency transient power is negative after forward faults, and positive after backward faults.
2) A novel directional pilot protection based on high-frequency transient power polarity is proposed. This method does not rely on line boundary conditions or system parameters, and eliminates the need for threshold value setting. This significantly reduces the burden on engineering personnel and is suitable for a wider range of scenarios.
3) A prototype device based on the proposed pilot protection is developed, and comprehensive hardware-in-loop (HIL) experiments sufficiently validate the effectiveness and superiority of the proposed method.

The rest of this article is organized as follows. Section II analyzes the polarity characteristics of high-frequency transient power during forward and backward faults, under different boundary conditions. Section III presents a directional pilot protection based on high-frequency transient power. In Section IV, the simulation case studies are carried out to validate the performance of the proposed protection. And in Section V, the protection prototype is developed, which is tested by HIL experimental cases. Finally, Section VI concludes this article.

## II. Fault Characteristics Under Different Line Boundary Conditions

This section analyzes the polarity characteristics of transient power after dc line faults, providing a theoretical foundation for the design of directional pilot protection. To discuss the characteristics of the transient power polarity under different boundary conditions, this analysis uses a three-terminal hybrid HVDC system shown in Fig. 1 as an example. In Fig. 1, $S_1$ represents a 12-pulse LCC station, whereas $S_2$ and $S_3$ denote the hybrid-bridge MMC stations. These are the most commonly

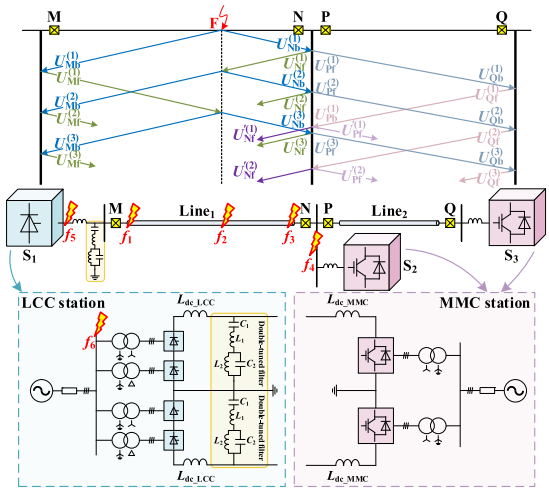


Fig. 1. Topology of a multiterminal hybrid HVDC (MTDC) system and lattice diagram of TWs after a DC fault.

used converter types in HVDC transmission systems. As illustrated, the system features three boundary conditions: the M port of $\text{Line}_1$ is equipped with a dc filter and a smoothing reactor as a boundary, the Q port of $\text{Line}_2$ is equipped with a current-limiting reactor as a boundary, while the N port of $\text{Line}_1$ and P port of $\text{Line}_2$ lack boundary elements. Above three boundary conditions encompass all possible line boundary scenarios in a dc system, allowing the relevant analytical conclusions to be applicable to various types of HVDC systems.

### *A. High-Frequency Power Characteristics Under Forward Faults*

According to circuit theory, the voltage $u$ and current $i$ on a uniform transmission line with unit length resistance $r$, inductance $L$, conductance $g$, and capacitance $C$ satisfy the following equation:

$$\begin{cases} \frac{\partial u}{\partial x} + L\frac{\partial i}{\partial t} + ri = 0 \\ \frac{\partial i}{\partial x} + C\frac{\partial u}{\partial t} + gu = 0. \end{cases} \tag{1}$$

In the frequency domain, (1) can be expressed as $-\mathrm{d}U(\mathrm{j}\omega)/\mathrm{d}x = ZI(\mathrm{j}\omega)$, $-\mathrm{d}I(\mathrm{j}\omega)/\mathrm{d}x = YU(\mathrm{j}\omega)$, where $Z = r + \mathrm{j}\omega L$, $Y = g + j\omega C$. For the sake of brevity, "$j\omega$" after the letter is omitted in the subsequent text, and only capital letters are used to denote physical quantities in the frequency domain. For dc lines, considering the coupling between the positive and negative poles, the positive and negative voltages $U_\mathrm{P}$ and $U_\mathrm{N}$, as well as the positive and negative currents $I_\mathrm{P}$ and $I_\mathrm{N}$, satisfy

$$\begin{cases} -\frac{d}{dx}\begin{bmatrix} U_P \\ U_N \end{bmatrix} = \begin{bmatrix} Z_s & Z_m \\ Z_m & Z_s \end{bmatrix}\begin{bmatrix} I_P \\ I_N \end{bmatrix} \\ -\frac{d}{dx}\begin{bmatrix} I_P \\ I_N \end{bmatrix} = \begin{bmatrix} Y_s & Y_m \\ Y_m & Y_s \end{bmatrix}\begin{bmatrix} U_P \\ U_N \end{bmatrix} \end{cases} \tag{2}$$

where $Z_s$, $Z_m$, $Y_s$, and $Y_m$ represent the self-impedance, mutual impedance, self-admittance, and mutual admittance of the line, respectively.

The solution to (2) is quite complex. Decoupling is typically achieved using the pole-to-mode transformation shown in the following:

$$\begin{bmatrix} U_0 \\ U_1 \end{bmatrix} = \frac{1}{\sqrt{2}}\begin{bmatrix} 1 & 1 \\ 1 & -1 \end{bmatrix}\begin{bmatrix} U_P \\ U_N \end{bmatrix}, \quad \begin{bmatrix} I_0 \\ I_1 \end{bmatrix} = \frac{1}{\sqrt{2}}\begin{bmatrix} 1 & 1 \\ 1 & -1 \end{bmatrix}\begin{bmatrix} I_P \\ I_N \end{bmatrix} \tag{3}$$

where $U_0$ and $U_1$ represent the 0-mode and 1-mode voltage, while $I_0$ and $I_1$ represent the 0-mode and 1-mode current. By combining (2) and (3), the general solution for the voltage and current can be expressed as follows:

$$\begin{cases} U_0(x) = F_0 e^{-\gamma_0 x} + B_0 e^{\gamma_0 x} \\ I_0(x) = \frac{F_0}{Z_0} e^{-\gamma_0 x} - \frac{B_0}{Z_0} e^{\gamma_0 x} \end{cases}, \quad \begin{cases} U_1(x) = F_1 e^{-\gamma_1 x} + B_1 e^{\gamma_1 x} \\ I_1(x) = \frac{F_1}{Z_1} e^{-\gamma_1 x} - \frac{B_1}{Z_1} e^{\gamma_1 x} \end{cases} \tag{4}$$

where $Z_0 = [(Z_\mathrm{s} + Z_\mathrm{m})/(Y_\mathrm{s} + Y_\mathrm{m})]^{0.5}$, $Z_1 = [(Z_\mathrm{s} - Z_\mathrm{m})/(Y_\mathrm{s} - Y_\mathrm{m})]^{0.5}$, $\gamma_0 = [(Z_\mathrm{s} + Z_\mathrm{m})(Y_\mathrm{s} + Y_\mathrm{m})]^{0.5}$, $\gamma_1 = [(Z_\mathrm{s} - Z_\mathrm{m})(Y_\mathrm{s} - Y_\mathrm{m})]^{0.5}$ represent the 0-mode wave impedance and propagation constant, as well as the 1-mode wave impedance and propagation constant. $F_0$ and $B_0$ denote the amplitudes of the forward and backward TWs of the 0-mode voltage, while $F_1$ and $B_1$ denote the amplitudes of the forward and backward TWs of the 1-mode voltage. The method proposed in this study is mainly designed in 1 mode. If not specified, all physical quantities in the following sections are 1-mode components and no longer labeled with the subscript "1."

From (4), in the mode domain, voltage and current can be decomposed into forward and backward TWs. Considering the propagation process of fault TWs, when a fault occurs in a dc line, a TW source is generated at the fault point within the fault component network. This TW propagates along the line to both ends, becoming the first incident wave (the first backward TW) at the endpoints. Simultaneously, the wave reflects at the endpoints, forming the first reflected wave (the first forward TW). The reflected wave is equal to the incident wave multiplied by the reflection coefficient. If there is a line on the other side of the endpoint, the incident wave will also cross the endpoint, creating the first refracted wave (the first forward TW of the adjacent line). As time progresses, the fault wave will undergo multiple reflections and refractions within the system; therefore, the voltage or current change at any point is the superposition of all forward and backward TWs at that point.

Fig. 1 illustrates the TW propagation process when a fault occurs at point F ($f_2$ for instance) on $\text{Line}_1$. This fault is a forward fault for the protections at M, N, and Q. In frequency domain, the transient voltage caused by the TW can be expressed as follows:

$$\Delta U_\mathrm{X} = \underbrace{U_\mathrm{Xb}^{(1)} + U_\mathrm{Xb}^{(2)} + U_\mathrm{Xb}^{(3)} + \cdots}_{\text{Incident wave at port X}} + \underbrace{U_\mathrm{Xf}^{(1)} + U_\mathrm{Xf}^{(2)} + U_\mathrm{Xf}^{(3)} + \cdots}_{\text{Reflected wave at port X}}$$

$$
\begin{aligned}
&+\underbrace{U'^{(1)}_{\mathrm{Xf}}+U'^{(2)}_{\mathrm{Xf}}+U'^{(3)}_{\mathrm{Xf}}+\ldots}_{\text{Refracted wave from Line}_2\text{ to Line}_1}\\
&=\underbrace{U^{(1)}_{\mathrm{Xb}}+U^{(2)}_{\mathrm{Xb}}+U^{(3)}_{\mathrm{Xb}}+\ldots}_{\text{Incident wave at port X}}\\
&+\underbrace{\beta_{\mathrm{X}}\cdot\overbrace{(U^{(1)}_{\mathrm{Xb}}+U^{(2)}_{\mathrm{Xb}}+U^{(3)}_{\mathrm{Xb}}+\ldots)}^{\text{Incident wave at port X}}}_{\text{Reflected wave at port X}}\\
&+\underbrace{A_{\mathrm{fb}}\cdot\overbrace{(U^{(1)}_{\mathrm{Xb}}+U^{(2)}_{\mathrm{Xb}}+U^{(3)}_{\mathrm{Xb}}+\ldots)}^{\text{Incident wave at port X}}}_{\text{Refracted wave from Lin e}_2\text{ to Line}_1}\\
&=(1+\beta_{\mathrm{X}}+A_{\mathrm{fb}})\cdot(U^{(1)}_{\mathrm{Xb}}+U^{(2)}_{\mathrm{Xb}}+U^{(3)}_{\mathrm{Xb}}+\ldots),\quad(5)
\end{aligned}
$$

where subscript X represents the protection at M, N, or Q, subscript b the backward TW, subscript f the forward TW, and superscript ($i$) represents the $i$th propagation of the TW. $\beta$ denotes the reflection coefficient at the protection position. $U_{\mathrm{Xf}}{}'^{(i)}$ represents the forward TW that is refracted from $U_{\mathrm{Xb}}{}^{(i)}$ to the adjacent line, then reflected back from the opposite end of the adjacent line, and subsequently refracted back to the original line. The definition of $I_{\mathrm{Xf}}{}'^{(i)}$ in (6) is similar to that of $U_{\mathrm{Xf}}{}'^{(i)}$. $A_{\mathrm{fb}}$ denotes the ratio of the same-time $U_{\mathrm{Xf}}{}'^{(i)}$ to $U_{\mathrm{Xb}}{}^{(i)}$. Accordingly, the transient current at protections M, N, and Q caused by the propagation of fault TW can be expressed as (6).

From Fig. 1, for the protections where adjacent lines do not exist (such as M and Q), $A_{\mathrm{fb}}=0$. For protection N, before the TW is refracted from Line$_2$ to Line$_1$, namely, during the interval $[t_0,\ t_0+2l_2/v)$ (where $t_0$ denotes the moment when the first travelling wave reaches protection N and $l_2$ represents the length of Line$_2$), $A_{\mathrm{fb}}$ can be considered to be zero. Consequently, (6) can be simplified to (7)

$$
\begin{aligned}
\Delta I_{\mathrm{X}}&=\underbrace{I_{\mathrm{Xb}(1)}+I^{(2)}_{\mathrm{Xb}}+I^{(3)}_{\mathrm{Xb}}+\ldots}_{\text{Incident wave at port X}}\\
&\quad+\underbrace{I^{(1)}_{\mathrm{Xf}}+I^{(2)}_{\mathrm{Xf}}+I^{(3)}_{\mathrm{Xf}}+\ldots}_{\text{Reflected wave at port X}}\\
&\quad+\underbrace{I'^{(1)}_{\mathrm{Xf}}+I'^{(2)}_{\mathrm{Xf}}+I'^{(3)}_{\mathrm{Xf}}+\ldots}_{\text{Refracted wave from Line}_2\text{ to Line}_1}\\
&=\underbrace{-1/Z_{\mathrm{C}}\cdot(U^{(1)}_{\mathrm{Xb}}+U^{(2)}_{\mathrm{Xb}}+U^{(3)}_{\mathrm{Xb}}+\ldots)}_{\text{Incident wave at port X}}\\
&\quad+\underbrace{1/Z_{\mathrm{C}}\cdot\beta_{\mathrm{X}}\cdot(U^{(1)}_{\mathrm{Xb}}+U^{(2)}_{\mathrm{Xb}}+U^{(3)}_{\mathrm{Xb}}+\ldots)}_{\text{Reflected wave at port X}}\\
&\quad+\underbrace{1/Z_{\mathrm{C}}\cdot A_{\mathrm{fb}}\cdot(U^{(1)}_{\mathrm{Xb}}+U^{(2)}_{\mathrm{Xb}}+U^{(3)}_{\mathrm{Xb}}+\ldots)}_{\text{Refracted wave from Line}_2\text{ to Line}_1}\\
&=(-1+\beta_{\mathrm{X}}+A_{\mathrm{fb}})/Z_{\mathrm{C}}\cdot(U^{(1)}_{\mathrm{Xb}}+U^{(2)}_{\mathrm{Xb}}+U^{(3)}_{\mathrm{Xb}}+\ldots)\\
&=\frac{-1+\beta_{\mathrm{X}}+A_{\mathrm{fb}}}{Z_{\mathrm{C}}\,(1+\beta_{\mathrm{X}}+A_{\mathrm{fb}})}\Delta U_{\mathrm{X}}.\qquad(6)
\end{aligned}
$$

TABLE I
PARAMETERS OF THE THREE-TERMINAL HYBRID DC SYSTEM

| Parameter | $S_1$ | $S_2$ | $S_3$ |
|---|---|---|---|
| rated DC voltage (kV) | ±805 | ±790 | ±785 |
| rated AC voltage (kV) | 525 | 525 | 525 |
| DC inductance (mH) | 150 | 75 | 75 |
| rated capacity (MVA) | 9720 | 3130 | 5100 |
| transformer leakage reactance (p.u.) | 0.2 | 0.165 | 0.21 |
| inductance of one arm (mH) | \ | 61.2 | 41.2 |
| SM capacitance ($\mu$F) | \ | 12 000 | 18 000 |
| number of SM in one arm | \ | 206 | 206 |
| series inductance of the filter (mH) | 4.443 | \ | \ |
| series capacitance of the filter ($\mu$F) | 7.916 | \ | \ |
| parallel inductance of the filter (mH) | 2.220 | \ | \ |
| parallel capacitance of the filter ($\mu$F) | 15.832 | \ | \ |

TABLE II
DC LINE PARAMETERS

| Parameter | Values |
|---|---|
| length of Line$_1$ and Line$_2$ (km) | 932, 557 |
| Height of conductors (m) | 41.33 |
| Horizontal spacing between conductors (m) | 22 |
| DC resistance of conductors (Ω/km) | 0.0459 |
| Outer radius of conductors (m) | 0.01812 |
| Sag of conductors (m) | 20 |
| Height of ground wires (m) | 58.33 |
| Horizontal spacing between ground wires (m) | 28 |
| DC resistance of ground wires (Ω/km) | 0.4696 |
| Outer radius of ground wires (m) | 0.007875 |
| Sag of ground wires (m) | 15 |

$$
\Delta I_{\mathrm{X}}=\frac{-1+\beta_{\mathrm{X}}}{Z_{\mathrm{C}}\,(1+\beta_{\mathrm{X}})}\Delta U_{\mathrm{X}}=\frac{-1+\frac{Z_{\mathrm{X}}-Z_{\mathrm{C}}}{Z_{\mathrm{X}}+Z_{\mathrm{C}}}}{Z_{\mathrm{C}}\left(1+\frac{Z_{\mathrm{X}}-Z_{\mathrm{C}}}{Z_{\mathrm{X}}+Z_{\mathrm{C}}}\right)}\Delta U_{X}=-\frac{\Delta U_{\mathrm{X}}}{Z_{\mathrm{X}}}\qquad(7)
$$

where $Z_{\mathrm{X}}$ represents the transient impedance observed from the line toward the back of the protection.

The polarity characteristics of the transient voltage and current are highly correlated with the phase characteristics of the transient impedance. The following sections analyze the phase-frequency characteristics of the transient impedance under different boundary conditions. According to the topology shown in Fig. 1, the reflection coefficients $\beta_{\mathrm{X}}$ at different locations can be calculated, allowing the transient impedances for the three boundary conditions to be derived as follows:

$$
Z_{\mathrm{M}}=Z_{\mathrm{filter}}\|\,(Z_{\mathrm{S1}}+\mathrm{j}\omega L_{\mathrm{dc\_S1}})\qquad(8)
$$

$$
Z_{\mathrm{N}}=Z_{\mathrm{C}}\|\,(Z_{\mathrm{S2}}+\mathrm{j}\omega L_{\mathrm{dc\_S2}})\qquad(9)
$$

$$
Z_{\mathrm{Q}}=Z_{\mathrm{S3}}+\mathrm{j}\omega L_{\mathrm{dc\_S3}}\qquad(10)
$$

where $Z_{\mathrm{S1}}$, $Z_{\mathrm{S2}}$, and $Z_{\mathrm{S3}}$ represent the equivalent impedances of converter stations $S_1$, $S_2$, and $S_3$, respectively, and their specific calculation methods are detailed in paper [19]. $L_{\mathrm{dc\_S1}}$, $L_{\mathrm{dc\_S2}}$, and $L_{\mathrm{dc\_S3}}$ are the dc inductances at the outlets of the three converter stations, respectively. $Z_{\mathrm{filter}}$ is the equivalent impedance of the double-tuned dc filter on the outlet of the LCC station. According to Fig. 1, $Z_{\mathrm{filter}}=\mathrm{j}\omega L_1+1/(\mathrm{j}\omega C_1)+(\mathrm{j}\omega L_2)\,\|\,(1/\mathrm{j}\omega C_2)$. $Z_{\mathrm{C}}$ denotes the line wave impedance [20].

Using the parameters of a specific three-terminal hybrid dc system in China (as listed in Tables I and II), the phase-frequency

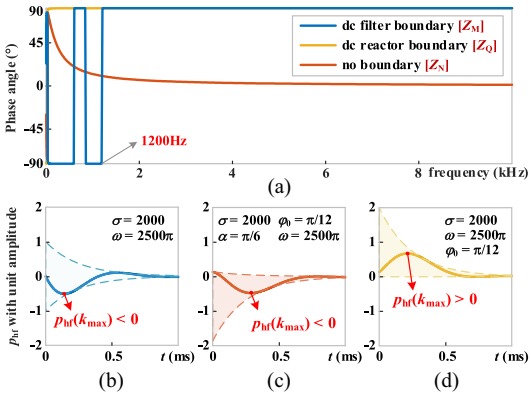


Fig. 2. Phase angle of transient impedance $Z_X$ and characteristic of high-frequency transient power $p_{hf}$. (a) The phase angle of the transient impedance $Z_X$ under different frequencies. (b) Normalized $p_{hf}$ under forward faults with boundary. (c) Normalized $p_{hf}$ under forward faults without boundary. (d) Normalized $p_{hf}$ under backward faults.

characteristics of the transient impedance are calculated and illustrated in Fig. 2(a).

For protection M, the line boundary consists of a dc filter and a smoothing reactor. Because the impedance of the smoothing reactor rapidly increases with the frequency, the transient impedance characteristics at M primarily depend on the characteristics of the lower-value filter impedance in the high-frequency range. The tuning frequencies of the double-tuned filter are 600 and 1200 Hz, designed to filter out the 12th and 24th harmonics, respectively [21]. Conventional double-tuned filters are composed solely of capacitive and inductive components [22], resulting in phase values of only $\pi/2$ and $-\pi/2$, with a sudden phase change occurring at each tuning frequency. As shown in Fig. 2(a), beyond 1200 Hz, the capacitive reactance of the filter becomes significantly smaller than its inductive reactance, resulting in a phase angle of $\pi/2$ for the transient impedance in the frequency range above 1200 Hz, indicating inductive characteristic.

For protection Q, the line boundary is a current-limiting reactor. The transient impedance $Z_Q$ comprises the reactor impedance and converter station impedance in series. As the frequency increases, the inductive components of the converter station impedance and current-limiting reactor gradually dominate. As illustrated in Fig. 2(a), in the high-frequency range, the phase angle of the transient impedance $Z_Q$ approaches $\pi/2$, displaying predominantly inductive characteristic.

In contrast, for the boundary-less scenario (taking protection N as an example), the phase angle of the transient impedance beside the protection gradually approaches 0° with frequency increasing, exhibiting resistive characteristic. This is because, in high-frequency range, $Z_{S2}+j\omega L_{dc\_S2}$ becomes much larger than the line wave impedance $Z_C$, rendering the transient impedance approximately equal to the resistive line wave impedance [23].

Therefore, according to (6), for scenarios in which the line has boundaries (such as with a filter and smoothing reactor or with only a current-limiting reactor), the transient current leads the transient voltage by $\pi/2$ in the high-frequency range (such as >1200 Hz). Differently, in the case of a boundary-less condition, the transient current leads the transient voltage by only a small phase angle $\alpha$ in high-frequency range, and $\alpha$ quickly approaches 0° as the frequency increasing.

The high-frequency components of voltage and current after a dc fault appear as quickly-attenuated signals in time domain. Let the high-frequency component of the transient voltage at port X be represented as $u_{X\text{-}hf} = U_{hf0}e^{-\sigma t}\sin(\omega t+\varphi_0)$. $U_{hf0}$ is the amplitude of the transient voltage signal, $\sigma$ is the attenuated coefficient, and $\varphi_0$ is the initial phase of the signal, with $0\le\varphi_0<2\pi$. Then, the high-frequency component of the current can be expressed as follows:

$$i_{X-hf} = \begin{cases} -\frac{U_{hf0}}{|Z_{X-hf}|}e^{-\sigma t}\sin(\omega t+\varphi_0-\frac{\pi}{2}), & \text{with boundary} \\ -\frac{U_{hf0}}{|Z_{X-hf}|}e^{-\sigma t}\sin(\omega t+\varphi_0-\alpha), & \text{no boundary} \end{cases} \tag{11}$$

where $i_{X\text{-}hf}$ represents the high-frequency component of the transient current at line port X and $|Z_{X\text{-}hf}|$ denotes the amplitude of the high-frequency transient impedance at port X. When X is M or Q, it corresponds to the case with boundary elements. When X = N, it represents the case without boundary. It is important to note that in the presence of boundary elements, the transient impedance is inductive, meaning that the high-frequency component of the transient current cannot experience abrupt change, and so its initial value is zero. Consequently, it can be deduced that the initial phase of the high-frequency voltage component is $\varphi_0 = \pi/2$, under the condition with boundary elements.

Furthermore, the high-frequency transient power caused by the fault TW can be expressed as follows:

$$p_{X-hf} = u_{X-hf}i_{X-hf}$$
$$= \begin{cases} \frac{0.5U_{hf0}^2}{|Z_{X-hf}|}e^{-2\sigma t}\cos\left(2\omega t+\frac{\pi}{2}\right), & \text{with boundary} \\ \frac{0.5U_{hf0}^2}{|Z_{X-hf}|}e^{-2\sigma t}\left[\cos\left(2\omega t+2\varphi_0-\alpha\right)-\cos\left(\alpha\right)\right], & \text{no boundary.} \end{cases} \tag{12}$$

According to (12), the characteristics of high-frequency transient power under forward faults can be obtained as follows. For scenarios where the line has boundaries, regardless of the attenuated coefficient $\sigma$, the high-frequency transient power reaches its maximum value $p_{hf}(k_{max})$ at $t = \pi/4\omega$ ($k_{max}$ indicates the moment when the high-frequency transient power achieves its maximum), as shown in Fig. 2(b). And the sign of the maximum value is negative.

For cases where the line lacks boundary, because $\alpha$ is a small value approaching zero, $\cos\alpha$ is a positive value greater than zero. Therefore, the expression $\cos(2\omega t + 2\varphi_0 - \alpha) - \cos\alpha$ becomes a cosine function shifted toward the negative half-axis. If the exponential decay term $e^{-2\sigma t}$ is ignored, the maximum value of $p_{hf}$ must be negative. When considering the $e^{-2\sigma t}$ term, it can be inferred from (12) that the polarity of $p_{hf}$ is also related to the initial phase $2\varphi_0 - \alpha$, frequency $f$, and attenuated coefficient $\sigma$. The coefficient $\sigma$ determines the order of appearance between the first crest and the first trough, with two extreme cases: when $2\varphi_0 - \alpha = \pi$, the first trough of the cosine function occurs at $t = 0$ and is unaffected by $e^{-2\sigma t}$. For $t > 0$, $p_{hf}$ will continuously decay

over time, resulting in a maximum value of $p_{\mathrm{hf}}$ that is necessarily negative. Conversely, when $2\varphi_0 - \alpha = 0$, the first crest appears at $t = 0$, followed by the first trough after half a cycle, which will be subject to exponential attenuation. Obviously, the smaller $f$ is, the longer the time interval between the crests and troughs, resulting in a greater amplitude difference between the two due to attenuation. Additionally, as the frequency decreases, $\alpha$ increases and $\cos\alpha$ decreases, leading to a reduced negative bias in the cosine function. In summary, when both $\sigma$ and $\alpha$ are large, $f$ is small, and $2\varphi_0 - \alpha = 0$, the negative polarity characteristic of the maximum value of $p_{\mathrm{hf}}$ will be most severely affected.

As discussed in the following, the frequency range of extracted high-frequency power is selected as 1.25–2.5 kHz. According to simulation results of faults at different locations, fit the extracted high-frequency voltage using $u_{\text{X-hf}} = U_{\mathrm{hf0}}\mathrm{e}^{-\sigma t}\sin(\omega t + \varphi_0)$. It can be found that, the attenuated coefficient $\sigma$ is always below 2000. And the value of $\alpha$ will not exceed $\pi/6$ under different system parameters. Therefore, considering the worst-case scenario, set $\sigma = 2000$, $\alpha = \pi/6$, $\omega = 2\pi \times 1250$, and $\varphi_0 = \alpha/2 = \pi/12$. The waveform of the high-frequency transient power under boundary-less condition is displayed as shown in Fig. 2(c). It indicates that, even in the worst-case scenario, the maximum value polarity of the high-frequency transient power remains negative. It should be noted that, the magnitude of the transient power does not affect its polarity characteristics. Thus, Fig. 2 presents the transient power curves with unit amplitude, that is, the amplitude is set to 1, considering only the exponential decay term and the cosine function term.

### *B. High-Frequency Power Characteristics Under Backward Faults*

For protection at P on $\mathrm{Line}_2$, the fault F is a backward fault. Similarly, the transient voltage and current at protection P caused by fault TW can be deduced as (13) and (14), where ${U_{\mathrm{Pf}}}'^{(i)}$ represents the forward TW generated by the reflection of $U_{\mathrm{Pf}}{}^{(i)}$ at terminal Q, which is then reflected again at terminal P. Similarly, ${i_{\mathrm{Pf}}}'^{(i)}$ is defined in the same manner. $A_{\mathrm{ff}}$ denotes the ratio of the same-time ${U_{\mathrm{Pf}}}'^{(i)}$ to $U_{\mathrm{Pf}}{}^{(i)}$

$$\begin{aligned}\Delta U_{\mathrm{P}} =& \underbrace{U_{\mathrm{Pf}}^{(1)} + U_{\mathrm{Pf}}^{(2)} + U_{\mathrm{Pf}}^{(3)} + \ldots}_{\text{Refracted wave from Line}_1\text{ to Line}_2} \\ &+ \underbrace{U_{\mathrm{Pb}}^{(1)} + U_{\mathrm{Pb}}^{(2)} + U_{\mathrm{Pb}}^{(3)} + \ldots}_{\text{Backward traveling wave reflected from Line}_2\text{ to port P}} \\ &+ \underbrace{U_{\mathrm{Pf}}'^{(1)} + U'(2)_{\mathrm{Pf}} + U'^{(3)}{}_{\mathrm{Pf}} + \ldots}_{\text{Reflected wave at port P on Line}_2} \\ =& \underbrace{U_{\mathrm{Pf}}^{(1)} + U_{\mathrm{Pf}}^{(2)} + U_{\mathrm{Pf}}^{(3)} + \ldots}_{\text{Refracted wave from Line}_1\text{ to Line}_2} \\ &+ \underbrace{A_{\mathrm{ff}} \cdot \overbrace{(U_{\mathrm{Pf}}^{(1)} + U_{\mathrm{Pf}}^{(2)} + U_{\mathrm{Pf}}^{(3)} + \ldots)}^{\text{Refracted wave from Line}_1\text{ to Line}_2}}_{\text{Backward traveling wave reflected from Line}_2\text{ to port P}} \\ &+ \underbrace{\beta_{\mathrm{P}} A_{\mathrm{ff}} \cdot \overbrace{(U_{\mathrm{Pf}}^{(1)} + U_{\mathrm{Pf}}^{(2)} + U_{\mathrm{Pf}}^{(3)} + \ldots)}^{\text{Refracted wave from Line}_1\text{ to Line}_2}}_{\text{Reflected wave at port P on Line}_2} \\ =& [1 + (1 + \beta_{\mathrm{P}})A_{\mathrm{ff}}] \cdot (U_{\mathrm{Pf}}^{(1)} + U_{\mathrm{Pf}}^{(2)} + U_{\mathrm{Pf}}^{(3)} + \ldots),\end{aligned} \tag{13}$$

$$\begin{aligned}\Delta I_{\mathrm{P}} =& \underbrace{I_{\mathrm{Pf}}^{(1)} + I_{\mathrm{Pf}}^{(2)} + I_{\mathrm{Pf}}^{(3)} + \ldots}_{\text{Refracted wave from Line}_1\text{ to Line}_2} \\ &+ \underbrace{I_{\mathrm{Pb}}^{(1)} + I_{\mathrm{Pb}}^{(2)} + I_{\mathrm{Pb}}^{(3)} + \ldots}_{\text{Backward traveling wave reflected from Line}_2\text{ to port P}} \\ &+ \underbrace{I_{\mathrm{Pf}}'^{(1)} + I_{\mathrm{Pf}}'^{(2)} + I_{\mathrm{Pf}}'^{(3)} + \ldots}_{\text{Reflected wave at port P on Line}_2} \\ =& \underbrace{1/Z_{\mathrm{C}} \cdot (U_{\mathrm{Pf}}^{(1)} + U_{\mathrm{Pf}}^{(2)} + U_{\mathrm{Pf}}^{(3)} + \ldots)}_{\text{Refracted wave from Line}_1\text{ to Line}_2} \\ &+ \underbrace{-1/Z_{\mathrm{C}} \cdot A_{\mathrm{ff}} \cdot \overbrace{(U_{\mathrm{Pf}}^{(1)} + U_{\mathrm{Pf}}^{(2)} + U_{\mathrm{Pf}}^{(3)} + \ldots)}^{\text{Refracted wave from Line}_1\text{ to Line}_2}}_{\text{Backward traveling wave reflected from Line}_2\text{ to port P}} \\ &+ \underbrace{1/Z_{\mathrm{C}} \cdot \beta_{\mathrm{P}} A_{\mathrm{ff}} \cdot \overbrace{(U_{\mathrm{Pf}}^{(1)} + U_{\mathrm{Pf}}^{(2)} + U_{\mathrm{Pf}}^{(3)} + \ldots)}^{\text{Refracted wave from Line}_1\text{ to Line}_2}}_{\text{Reflected wave at port P on Line}_2} \\ =& (1 - A + \beta_{\mathrm{P}} A)/Z_{\mathrm{C}} \cdot (U_{\mathrm{Pf}}^{(1)} + U_{\mathrm{Pf}}^{(2)} + U_{\mathrm{Pf}}^{(3)} + \ldots) \\ =& \frac{1 - A + \beta_{\mathrm{P}} A}{Z_{\mathrm{C}}(1 + A + \beta_{\mathrm{P}} A)} \Delta U_{\mathrm{P}},\end{aligned} \tag{14}$$

Before the TW reflected from opposite terminal Q returns to port P, namely, during the interval $[t_0, t_0{+}2l_2/v)$, $A_{\mathrm{ff}}$ can be considered to be zero. Consequently, (14) can be simplified to

$$\Delta I_{\mathrm{P}} = \Delta U_{\mathrm{P}}/Z_{\mathrm{C}}. \tag{15}$$

In the high-frequency range, the line wave impedance $Z_{\mathrm{C}}$ approaches a real number and exhibits resistive characteristics [20]. Therefore, according to (15), the transient current is in phase with the transient voltage in the high-frequency range.

Let the high-frequency component of the transient voltage at protection P be represented as $u_{\text{P-hf}} = U_{\mathrm{hf0}}\mathrm{e}^{-\sigma t}\sin(\omega t{+}\varphi_0)$. The corresponding high-frequency transient current at the same frequency can be expressed as follows:

$$i_{\mathrm{P-hf}} = (U_{\mathrm{hf0}}/Z_{\mathrm{C-hf}})\,\mathrm{e}^{-\sigma t}\sin(\omega t + \varphi_0), \tag{16}$$

where $Z_{\text{C-hf}}$ represents the line wave impedance in the high-frequency range. It should be pointed out that, because (15) does not include the reflection and refraction coefficients at the ports, the relationship between the voltage and current in the case of backward faults is independent of the presence of boundary elements. Thus, (15) is also applicable for analyzing the backward fault conditions at protections M and Q.

Furthermore, the high-frequency transient power caused by the TW can be expressed as follows:

$$p_{\mathrm{P-hf}} = u_{\mathrm{P-hf}} i_{\mathrm{P-hf}} = \frac{0.5U_{\mathrm{hf0}}^2}{Z_{\mathrm{C-hf}}} \mathrm{e}^{-2\sigma t}[1-\cos(2\omega t + 2\varphi_0)]. \tag{17}$$

Obviously, in the case of a backward fault, the high-frequency transient power is always greater than or equal to zero, meaning with a positive maximum value, as shown in Fig. 2(d).

## III. Directional Pilot Protection Based on High-Frequency Transient Power

According to the above analysis, regardless of the boundary conditions, the polarity of the maximum value of high-frequency transient power after forward faults in a dc system is always negative, whereas it is positive after backward faults. By utilizing these characteristics, a settling-less directional pilot protection that does not dependent on line boundaries or system parameters can be designed.

### A. Designed Fault Direction Criterion

There are various mathematical methods for extracting high-frequency components, and this paper employs the commonly used wavelet transform. In practical engineering, the Mallat algorithm is a widely utilized discrete wavelet transform algorithm, with its computation formula given by

$$\begin{cases} a_j(k) = \sum_n a_{j-1}(n)\, h_0(n-2k) \\ d_j(k) = \sum_n a_{j-1}(n)\, h_1(n-2k) \end{cases} \tag{18}$$

where $h_0$ and $h_1$ represent the low-pass and high-pass filter array, respectively, $a_j(k)$ is defined as the approximate coefficient that reflects the low-frequency information of the signal, and $d_j(k)$ is defined as the detail coefficient that reflects the high-frequency information, respectively. When the sampling frequency is $f_{\mathrm{s}}$, the sampled voltage signal $u(k)$ is the initial wavelet transform signal $a_0(k)$. $a_j(k)$ represents the approximate coefficient after the $j$th wavelet transform, which reflects the transient voltage information in the frequency range of $0 \sim f_{\mathrm{s}}/2^{j+1}$. While $d_j(k)$ represents the detail coefficient after the $j$th wavelet transform, reflecting the transient voltage information in the frequency range of $f_{\mathrm{s}}/2^{j+1} \sim f_{\mathrm{s}}/2^{j}$. The same principle applies when performing wavelet transform on sampled current signals.

After performing a $j$th wavelet transform on the sampled voltage $u(k)$ and current $i(k)$, their high-frequency components can be denoted as $u_{\mathrm{d}j}(k)$ and $i_{\mathrm{d}j}(k)$, respectively. And the high-frequency transient power $p_{\mathrm{hf}}$ can be calculated as follows:

$$p_{\mathrm{hf}}(k) = u_{\mathrm{d}j}(k) i_{\mathrm{d}j}(k). \tag{19}$$

To mitigate the effects of noise and other interference signals, this study selects the 2nd level detail coefficients as the high-frequency components used in the protection criterion, considering the frequency division characteristic of the discrete wavelet transform. At present, most dc protection devices are configured at sampling rates of 10 or 20 kHz [23]. Therefore, the frequency range corresponding to 2nd level detail coefficients is [1.25, 2.5 kHz] or [2.5, 5 kHz]. Accordingly, the length of the data window for extracting high-frequency components can be set as 2 ms (including 1 ms before the protection start moment and 1 ms after). Furthermore, since the 1-mode parameters of the line are minimally affected by frequency variations [14], this study uses the 1-mode voltage $u_1(k)$ and current $i_1(k)$ to calculate the high-frequency transient power.

As analyzed, the polarity of maximum value of high-frequency transient power can be used to identify the fault direction. Therefore, using the maximum value (with sign) of the extracted high-frequency transient power $p_{\mathrm{hf}}(k_{\max})$, a direction criterion can be designed as follows:

$$K_{\mathrm{dr}} = \frac{p_{\mathrm{hf}}(k_{\max})}{|p_{\mathrm{hf}}(k_{\max})|} = \begin{cases} -1 & \Rightarrow \text{Forward fault} \\ 1 & \Rightarrow \text{Backward fault} \end{cases} \tag{20}$$

where $K_{\mathrm{dr}}$ represents the polarity of the high-frequency transient power.

Note that this criterion can correctly identify the fault direction during the interval $[t_0, t_0 + 2l_2/v)$ after a fault. After $t_0 + 2l_2/v$, although the reflected travelling waves from adjacent lines may cause a change in the polarity of the high-frequency transient power, the rapid decay of the high-frequency signals over time ensures that the maximum value of the high-frequency transient power occurs during the initial transient period. Therefore, the subsequent wave reflection and refraction processes do not affect the validity of this criterion.

### B. Selection of the Frequency Range

According to the previous analysis, the higher the frequency range selected in (19), the more evident the polarity characteristic of the transient power, resulting in a better performance of criterion (20). However, a higher frequency range requires a higher sampling rate. Increased sampling rates are more susceptible to high-frequency noise, which can significantly affect the performance of dc protections. So it is essential to select an appropriate frequency range used in the protection.

For backward faults, since the 1-mode wave impedance of the line exhibits resistive characteristic at frequencies above about 100 Hz [20], this section primarily analyses the phase-frequency characteristics of the transient impedance during forward faults. Given that the equivalent impedances of the LCC and MMC stations are predominantly inductive at higher frequencies, their equivalent resistances can be considered negligible. Thus, in the high-frequency range, $Z_{\mathrm{S1}}$, $Z_{\mathrm{S2}}$, and $Z_{\mathrm{S3}}$ can be represented by $\mathrm{j}\omega L_{\mathrm{S1}}$, $\mathrm{j}\omega L_{\mathrm{S2}}$, and $\mathrm{j}\omega L_{\mathrm{S3}}$, respectively [24], [25]. According to (10), we obtain $Z_{\mathrm{Q}} = \mathrm{j}\omega(L_{\mathrm{S3}} + L_{\mathrm{dc\_S3}})$. Therefore, $Z_{\mathrm{Q}}$ in Fig. 2(a) exhibits almost purely inductive characteristics. From (8) and (9), we derive $Z_{\mathrm{M}} = Z_{\mathrm{filter}} \parallel [\mathrm{j}\omega(L_{\mathrm{S1}} + L_{\mathrm{dc\_S1}})]$ and $Z_{\mathrm{N}} = Z_{\mathrm{C}} \parallel [\mathrm{j}\omega(L_{\mathrm{S2}} + L_{\mathrm{dc\_S2}})]$. Keeping $Z_{\mathrm{filter}}$ and $Z_{\mathrm{C}}$ unchanged, let the value of the parallel inductive component $(L_{\mathrm{S}} + L_{\mathrm{dc}})$ vary in increments of 80 mH within the range of 80–400 mH. This range encompasses most parameters that can be selected for converter stations and dc inductors in practical dc engineering [23]. The phase-frequency characteristics of $Z_{\mathrm{M}}$ and $Z_{\mathrm{N}}$ can be obtained as shown in Fig. 3(a) and (b), respectively. The red curves in Fig. 3(a) and (b) represent the phase-frequency characteristics of the dc filter and the 1-mode wave impedance, respectively.

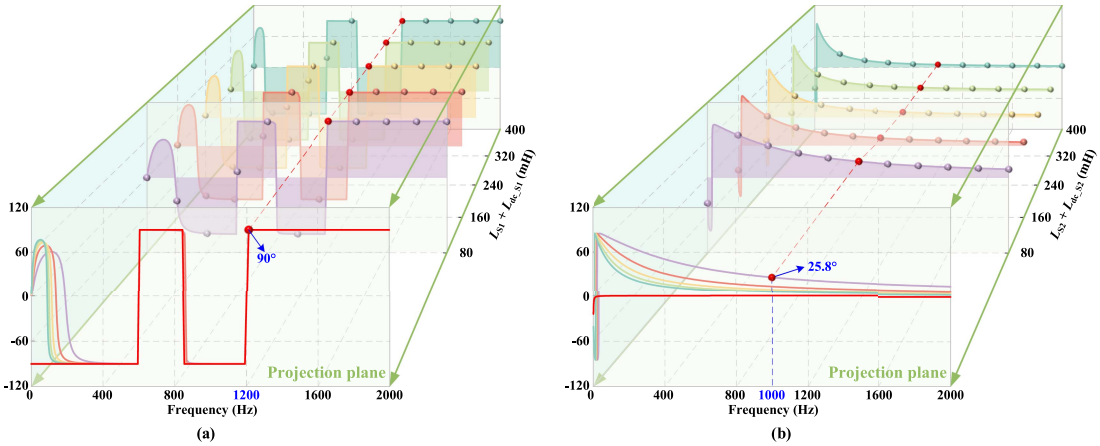


Fig. 3. Phase-frequency characteristic curves of $Z_M$ and $Z_N$ with different values of ($L_S$+$L_{dc}$). (a) Phase angle of $Z_M$. (b) Phase angle of $Z_N$.

As shown in Fig. 3(a), for cases where the filter serves as the boundary, changes in the parallel reactance only affect the phase-frequency characteristics of $Z_M$ in the low-frequency range. In high-frequency range (e.g., $>$ 400 Hz), the phase-frequency characteristics of $Z_M$ are almost unaffected and closely align with those of the filter impedance $Z_{filter}$. This is because, as the frequency increases, the magnitude of $Z_{filter}$ becomes significantly smaller than that of the parallel reactance, resulting in the measured impedance being approximately equal to $Z_{filter}$. Therefore, in this case, the selection of the frequency range should primarily consider the frequency at which the filter exhibits purely inductive characteristics, and it is 1200 Hz for the double-tuned filter and 1800 Hz for the triple-tuned filter.

As shown in Fig. 3(b), changes in the parallel reactance have a minimal effect on the phase-frequency characteristics of $Z_N$ in high-frequency range. According to (9), as the frequency increases, the parallel reactance increases, whereas the magnitude of $Z_C$ remains relatively constant, causing $Z_N$ to approach the line wave impedance $Z_C$. When the frequency exceeds 1000 Hz, the phase of $Z_N$ remains below 30°, resulting in $\cos\alpha > \sqrt{3}/2$. Under this condition, the negative polarity characteristic of the maximum value in the boundary-less case described in (12) becomes sufficiently pronounced. In other words, in this scenario, a frequency range greater than 1 kHz is adequate. In summary, as mentioned in Section III-A, extracting frequencies above 1.25 kHz is reasonable for the scenarios discussed in this study. While for systems equipped with a triple-tuned filter, the frequency range should be greater than 1800 Hz.

It should be noted that the direction criterion (20) is proposed based on the frequency domain characteristics of the system parameters such as $Z_X$ and $Z_C$, but the method proposed in this study does not rely on these system parameters and is not affected by the time-varying characteristics of the system parameters. This is because the calculation of $Z_X$ and $Z_C$ is well-founded theoretically [19], [20], [24], [25]. On this basis, it can be seen from Figs. 2 and 3, as well as paper [20], that the variation of the system parameters does not affect the characteristic that the $Z_X$ and $Z_C$ phases remain essentially unchanged in the high-frequency range. Equation (19) takes full advantage of this stable feature by extracting high-frequency power. Furthermore, the computation of (19) only requires voltage and current sampling data without the need to calculate $Z_X$ and $Z_C$. Therefore, the proposed method does not rely on system parameters, ensuring higher reliability engineering practicality.

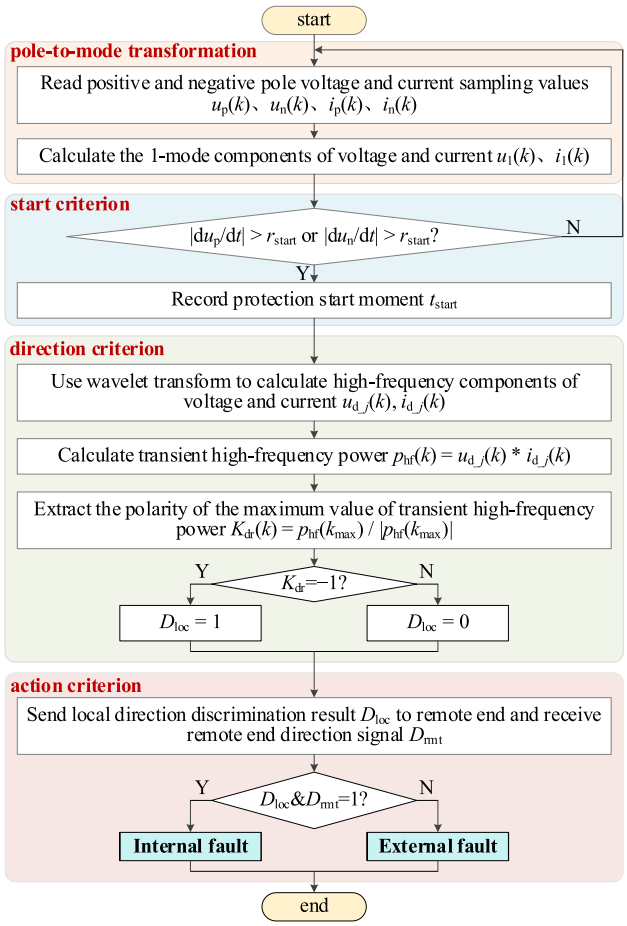


Fig. 4. Flowchart of the proposed directional pilot protection.

## C. Algorithm of the Proposed Directional Pilot Protection

Based on the proposed direction criterion, this section presents the design of a directional pilot protection scheme, as illustrated in Fig. 4. This scheme includes a start criterion based

on the voltage derivative, a directional criterion based on the high-frequency transient power, and a final pilot action criterion. The specific steps are as follows.

*Step 1:* Read and record the sampling data, including the sampled values of the positive and negative pole voltages and currents $u_{\mathrm{p}}(k)$, $u_{\mathrm{n}}(k)$, $i_{\mathrm{p}}(k)$, and $i_{\mathrm{n}}(k)$. Calculate the 1-mode components of the voltage and current, $u_1(k)$ and $i_1(k)$.

*Step 2:* Based on the sampled values of the positive and negative pole voltages $u_{\mathrm{p}}(k)$ and $u_{\mathrm{n}}(k)$, the protection start criterion is implemented using the change of voltage

$$|du/dt| = |u(k) - u(k-1)| \cdot f_s > r_{\mathrm{start}} \tag{21}$$

where $r_{\mathrm{start}}$ represents the threshold value of the starting criterion. When the voltage derivative of any pole exceeds the start threshold for three consecutive times, the protection is started. The number of sampling data corresponding to the starting time is recorded (using the first time when the threshold is exceeded).

*Step 3:* After the protection being started, the direction criterion based on the high-frequency transient power polarity is used to identify the fault direction [described as (20)]. If the criterion indicates a forward fault, set the local fault direction indication signal $D_{\mathrm{loc}}$ to 1.

*Step 4:* The local direction indication result $D_{\mathrm{loc}}$ is sent to the remote end and the remote direction signal $D_{\mathrm{rmt}}$ is received. As shown in (22), according to the direction indication results from both ends, determine whether protection should operate

$$\begin{cases} \boldsymbol{D}_{\mathrm{loc}} \& \boldsymbol{D}_{\mathrm{rmt}} = 1 \Rightarrow \text{internal fault} \\ \boldsymbol{D}_{\mathrm{loc}} \& \boldsymbol{D}_{\mathrm{rmt}} = 0 \Rightarrow \text{external fault.} \end{cases} \tag{22}$$

It should be noted that the method proposed in this study is a directional pilot protection, which only transmits logical signals and does not require data synchronization. Consequently, the communication costs and complexity are relatively low. Additionally, the communication delay only affects the operation speed of the protection and will not compromise the accuracy of the protection. However, it is crucial to acknowledge that, any communication failure will render the pilot protection ineffective. From the perspective of protection scheme design in practical engineering, to ensure reliability, it is often necessary to configure primary and backup protection schemes. In various scenarios, combinations and configurations of single-ended protection, directional pilot protection, and current differential protection can be effectively utilized. When communication failures prevent reliable operation of the pilot protection, alternative methods such as single-ended protection or handshaking techniques [26] can be employed for fault isolation.

### D. Complexity Evaluation of the Proposed Algorithm

The algorithm proposed in this article utilizes wavelet transform (18) to calculate the 2nd level detail coefficients, enabling the extraction of high-frequency transient power corresponding to specific frequency bands. Compared to protections based on time-domain information, this approach increases the computational load of the algorithm, making it essential to evaluate the impact of introducing wavelet transform on the operation speed of protection.

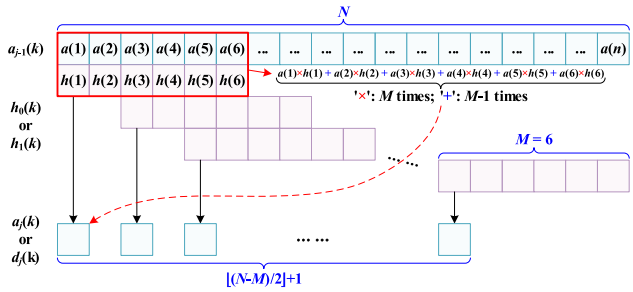


Fig. 5. Computation process of wavelet transform.

As shown in (18), the implementation of wavelet transform in the protection device essentially involves the sliding inner product of the wavelet filter array with the sampled signal. The downsampling process required by the wavelet transform is equivalent to sliding two data points at each step. Fig. 5 illustrates the computation process of the wavelet transform (using the "db3" wavelet for instance). In Fig. 5, $N$ represents the length of the protection data window, and $M$ denotes the length of the wavelet filter array. As showing, each wavelet transform (inner product) consists of $M$ multiplications and $M-1$ additions. After completing each inner product, the filter array slides forward by two data points, and the corresponding sampled data is again subjected to an inner product. This process continues as the filter array slides from start to finish, completing one level of wavelet decomposition for the entire analyzed data window, which includes a total of $M \cdot \lfloor (N-M)/2+1 \rfloor$ multiplications and $(M-1) \cdot \lfloor (N-M)/2+1 \rfloor$ additions, where $\lfloor \cdot \rfloor$ represents rounding down. In the 2nd level of decomposition, the data to be decomposed consists of $\lfloor (N-M)/2+1 \rfloor$ points obtained from the first decomposition. Consequently, the total number of computations required for the first two wavelet transforms can be calculated as follows:

$$\begin{cases} '\times': & M\left\lfloor \frac{3\lfloor (N-M)/2+1 \rfloor - M}{2} + 1 \right\rfloor \\ '+': & (M-1)\left\lfloor \frac{3\lfloor (N-M)/2+1 \rfloor - M}{2} + 1 \right\rfloor. \end{cases} \tag{23}$$

Taking the protection algorithm with a signal sampling rate of 10 kHz as an example, the data window is selected to be from 1 ms before to 1 ms after the protection start time, resulting in a protection data window length of $N = 20$. The length of the "db3" wavelet filter array is $M = 6$. Thus, according to (23), the wavelet transform in the protection algorithm comprises a total of 60 multiplications and 50 additions.

In fact, for the proposed method, the authors have developed a corresponding dc directional pilot protection device, and the relevant experimental results will be presented in Section V. This protection device is developed based on the dc protection hardware platform of a manufacturer in China, employing the P1010 processor with a clock frequency of 800 MHz, resulting in a clock period of 1 / (800 MHz) = 1.25 ns. When considering the computation process independently, a single addition operation, which includes assignment and summation, takes approximately 3 clock cycles (i.e., 3.75 ns). A single multiplication operation, which involves assignment, shifting, and multiple summations,

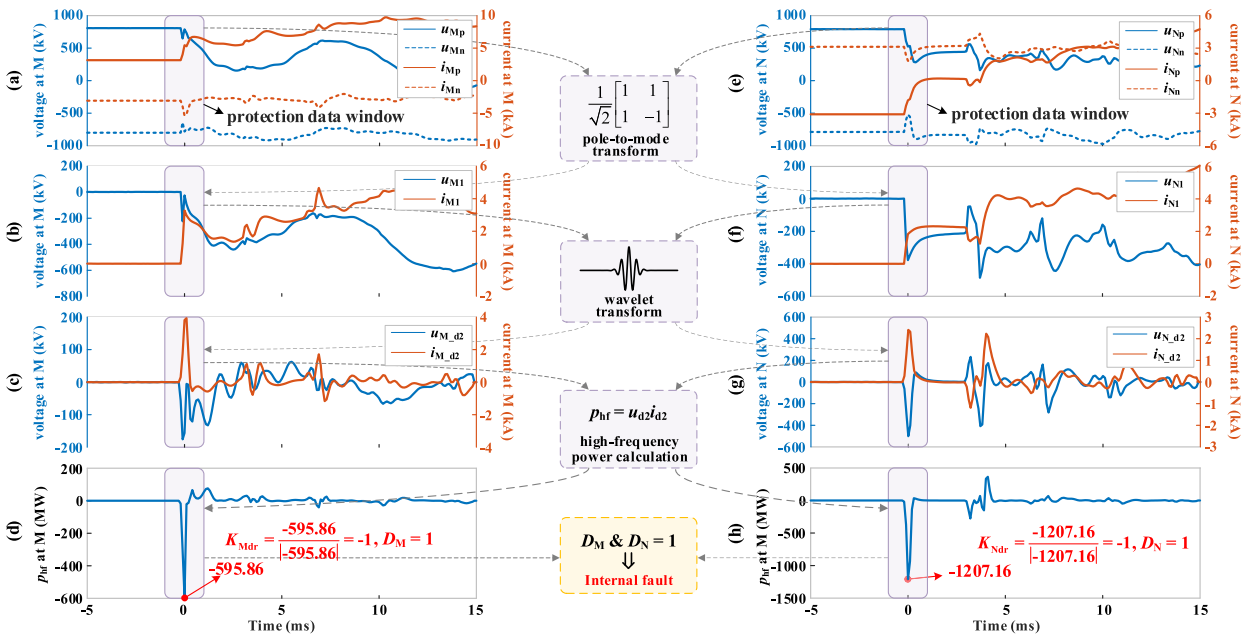


Fig. 6. Operation performance of protection M and N after internal positive pole-to-ground fault ($f_2$). (a) Measured voltage and current at M. (b) 1-mode voltage and current at M. (c) High-frequency voltage and current at M. (d) High-frequency power at M. (e) Measured voltage and current at N. (f) 1-mode voltage and current at N. (g) High-frequency voltage and current at N. (h) High-frequency power at N.

takes about 10 clock cycles (i.e., 12.5 ns). Therefore, performing 60 multiplications and 50 additions requires approximately 0.94 $\mu$s in total. Compared to the 1 ms data window after protection start, the relay operating time of 500 $\mu$s, and communication delay ranging from several milliseconds to tens of milliseconds, the computation time required for the wavelet transform is sufficiently small and can be considered negligible in relation to the overall operation time of the protection device.

Additionally, with the support of hardware multipliers and compiler optimizations, a single instruction that includes both addition and multiplication can be optimized, further reducing the required clock cycles. Thus, it can be concluded that the additional computational load and delay introduced by the wavelet transform in the dc protection device are entirely acceptable.

## IV. Simulation Case Study

To validate the performance of the proposed protection, this section establishes a ±800 kV three-terminal hybrid dc transmission system simulation model based on the PSCAD/EMTDC, as shown in Fig. 1. Terminal $S_1$ is an LCC station equipped with a 150 mH smoothing reactor and a double-tuned filter. Terminals $S_2$ and $S_3$ are MMC stations, each equipped with a 75 mH current-limiting reactor. The detailed parameters of the converter stations are listed in Table I. Both $\text{Line}_1$ and $\text{Line}_2$ are modelled as frequency-dependent dc overhead lines, with detailed parameters listed in Table II.

### A. Feasibility of the Proposed Protection

To validate the feasibility of the proposed protection, we set a metallic positive-pole-to-ground fault at position $f_2$ on $\text{Line}_1$.

The signal sampling rate is 10 kHz, and the second level "db3" wavelet transform is applied to the 1-mode measured voltage and current signals to extract the high-frequency components in the range of 1.25–2.5 kHz.

*1) Internal Fault:* For protections M and N, the fault at $f_2$ is internal. The corresponding results are shown in Fig. 6 (the start time of the protection is set as 0 ms). After the protections M and N are immediately started after the fault, the high-frequency components of the 1-mode voltage and current are extracted using the wavelet transform, and the corresponding high- frequency transient power is calculated. Notably, the proposed protection criterion requires only 1 ms of data before and 1 ms of data after being started, to identify the fault direction. However, to observe the complete characteristics of the high-frequency components of voltage and current, as well as the high-frequency transient power during the fault process, the results for 5 ms before and 15 ms after the fault are displayed in the figure.

From Fig. 6, at protection M, the maximum values of the high-frequency voltage component $u_{\text{M\_d2}}$ and high-frequency current component $i_{\text{M\_d2}}$ have opposite polarities. This is because affected by the dc filter boundary, the phase angle of the high-frequency transient impedance $Z_{\text{M}}$ approaches 90° during a forward fault. As previously analyzed, the initial phase of the high-frequency voltage is approximately 90°, whereas that of the high-frequency current is approximately –180°. Consequently, the high-frequency transient power reaches its maximum value with negative polarity one-quarter of a cycle after the fault. As shown in Fig. 6(d), $K_{\text{Mdr}} = -595.86/595.86 = -1$, indicating that M identifies the fault as a forward fault ($D_{\text{M}} = 1$). At protection N, there is no boundary element behind it, and the phase angle of the high-frequency transient impedance $Z_{\text{N}}$ approaches 0°. According to (11), a high-frequency transient current leads to a transient voltage of approximately 180°. In this case, the transient power reaches its maximum value with negative polarity half a cycle after the fault. As shown in

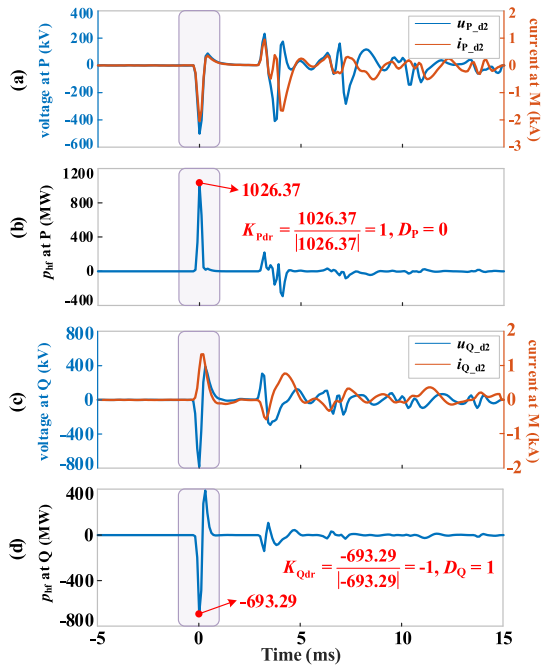


Fig. 7. Simulation results of P and Q after an external positive pole-to-ground fault ($f_2$). (a) Measured voltage and current at P. (b) High-frequency power at P. (c) Measured voltage and current at Q. (d) High-frequency power at Q.

Fig. 6(h), $K_{Ndr} = -1207.16 / 1207.16 = -1$, which also indicates a forward fault ($D_N = 1$). Finally, because $D_M \,\&\, D_N = 1 \,\&\, 1 = 1$, protections M and N identify the fault as internal.

*2) External Fault:* For protections P and Q, the fault at $f_2$ is an external fault. The corresponding simulation results are presented in Fig. 7. It can be observed that, for protection P, the maximum value polarities of the high-frequency transient voltage $u_{P\_d2}$ and current $i_{P\_d2}$ within the observation window are the same. This is because during a backward fault, regardless of the presence of boundaries, the high-frequency transient impedance behaves similar to the wave impedance of the overhead line, exhibiting resistive characteristic. Consequently, phases of $u_{P\_d2}$ and $i_{P\_d2}$ are essentially aligned. And the maximum value of the high-frequency power within the observed data window displays a positive polarity. By calculating $K_{Pdr} = 1026.37/1026.37 = 1$, protection P identifies the fault as backward ($D_P = 0$). For protection Q, which has a current-limiting reactor as a boundary, the fault at $f_2$ is forward, and the maximum value of the high-frequency transient power within the data window has a negative polarity. By calculating $K_{Qdr} = -1207.16/1207.16 = -1$, it identifies the fault as forward ($D_Q = 1$). Finally, $D_P \,\&\, D_Q = 0 \,\&\, 1 = 0$, the protections P and Q identify the fault as an external one.

### B. Performance Under Different Kinds of Faults

The aforementioned cases of internal and external faults validate the effectiveness of the proposed protection under different boundary conditions. To further evaluate the operation performance of the proposed method, faults with various locations and different transition resistances are introduced into the system,

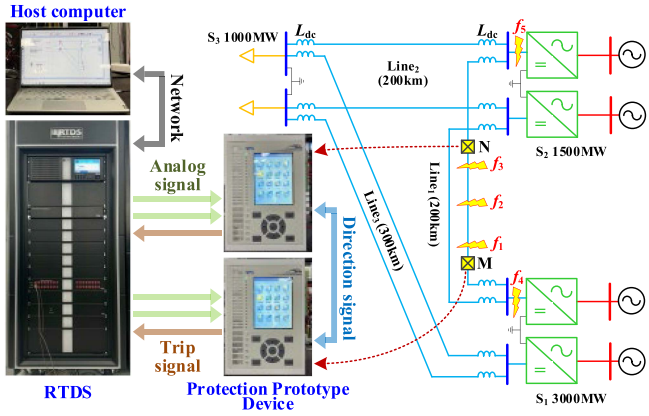


Fig. 8. Hardware-in-loop test system.

and 20 dB Gaussian white noise is applied to the sampled signals. The simulation results are listed in Table III. According to the test results, the proposed method demonstrates fast and reliable operation under various fault conditions. The correctness of the operation results is maintained even in the presence of high-resistance faults and considerable noise interference. This demonstrates the sensitivity and reliability of the proposed protection.

## V. Hardware-in-Loop Experiment Test

According to the proposed method, the directional pilot protection prototype device is developed on the DCP3 protection platform of Tianjin Keyvia Electric Co., Ltd, with the sampling rate of 10 kHz. In addition, a HIL experiment testing platform is constructed based on the real-time digital simulator (RTDS) platform, as shown in Fig. 8. Because the authors are authorized for only two cores in the RTDS, the computational ability is limited. Therefore, a three-terminal dc system is established, with terminal $S_3$ simplified to a 1000 MW dc load to reduce the computational burden. The geometric parameters of the lines are consistent with those in Table II, whereas the parameters for the half-bridge MMC converter stations $S_1$ and $S_2$ are provided in Table IV.

As shown in Fig. 8, two boundary conditions for the dc line are considered, i.e., there are no boundary elements at either end of the line ($L_{dc} = 0$), and there are $L_{dc} = 150$ mH dc inductors at both ends. The faults are set at different locations ($f_1$–$f_5$) and the operation performance of the protection prototype is observed. Each fault scenario is repeated in five independent tests, resulting in 300 sets of experimental test results, as listed in Table V. In Table V, $t_{op\_M}$ and $t_{op\_N}$ are the times from the fault occurrence to the moment the RTDS platform receives trip signals from the protections on both sides.

The test results indicate that, for faults $f_1$–$f_3$ occurring on $Line_1$, regardless of the presence of boundary elements, the maximum values of the high-frequency transient power measured by protections at both ends consistently exhibit negative polarity, allowing them to classify the fault as an internal fault. In most cases, the protection can operate within 4 ms (including the time required for the trip relay output, but ignoring the

TABLE III
SIMULATION RESULTS UNDER DIFFERENT FAULT CONDITIONS

| Fault Type | Fault Location | Fault Resistance (Ω) | Noise (dB) | $p_{M\ hf}(k_{max})$, $p_{N\ hf}(k_{max})$ (MW) | $D_M$ & $D_N$ | Result of Protection M, N | $p_{P\ hf}(k_{max})$, $p_{Q\ hf}(k_{max})$ (MW) | $D_P$ & $D_Q$ | Result of Protection P, Q |
|---|---|---|---|---|---|---|---|---|---|
| pole-to-ground | $f_1$ | 0 | 0 | −21315, −2391.5 | 1 & 1 = 1 | internal | 1964.9, −1259.5 | 0 & 1 = 0 | external |
| | | 0 | 20 | −21120, −2425.8 | 1 & 1 = 1 | internal | 2013.3, −1235.8 | 0 & 1 = 0 | external |
| | | 500 | 0 | −59.36, −6.994 | 1 & 1 = 1 | internal | 5.197, −4.405 | 0 & 1 = 0 | external |
| | $f_2$ | 0 | 0 | −595.9, −1207.2 | 1 & 1 = 1 | internal | 1026.4, −693.3 | 0 & 1 = 0 | external |
| | | 0 | 20 | −483.8, −1190.8 | 1 & 1 = 1 | internal | 1080.5, −706.6 | 0 & 1 = 0 | external |
| | | 500 | 0 | −36.13, −73.56 | 1 & 1 = 1 | internal | 62.10, −42.26 | 0 & 1 = 0 | external |
| | $f_3$ | 0 | 0 | −648.5, −2354.2 | 1 & 1 = 1 | internal | 1780.4, −1105.3 | 0 & 1 = 0 | external |
| | | 0 | 20 | −714.8, −2255.6 | 1 & 1 = 1 | internal | 1802.1, −1101.9 | 0 & 1 = 0 | external |
| | | 500 | 0 | −29.01, −105.8 | 1 & 1 = 1 | internal | 79.18, −47.37 | 0 & 1 = 0 | external |
| | $f_4$ | 0 | 0 | −648.6, 1782.8 | 1 & 0 = 0 | external | 1783.2, −1105.0 | 0 & 1 = 0 | external |
| | | 0 | 20 | −657.7, 1835.3 | 1 & 0 = 0 | external | 1746.7, −1099.4 | 0 & 1 = 0 | external |
| | | 500 | 0 | −28.95, 78.81 | 1 & 0 = 0 | external | 78.96, −47.04 | 0 & 1 = 0 | external |
| | $f_5$ | 0 | 0 | 87.75, −74.26 | 0 & 1 = 0 | external | 36.79, −34.25 | 0 & 1 = 0 | external |
| | | 500 | 0 | 1.879, −1.539 | 0 & 1 = 0 | external | 1.182, −0.898 | 0 & 1 = 0 | external |
| pole-to-pole | $f_1$ | 0 | 0 | −90077, −10064 | 1 & 1 = 1 | internal | 8270.4, −5409.1 | 0 & 1 = 0 | external |
| | | 0 | 20 | −90951, −10151 | 1 & 1 = 1 | internal | 8163.4, −5283.1 | 0 & 1 = 0 | external |
| | | 500 | 0 | −88.04, −864.4 | 1 & 1 = 1 | internal | 67.74, −55.16 | 0 & 1 = 0 | external |
| | $f_2$ | 0 | 0 | −4292.5, −8656.2 | 1 & 1 = 1 | internal | 7370.4, −4956.4 | 0 & 1 = 0 | external |
| | | 0 | 20 | −4141.6, −8476.4 | 1 & 1 = 1 | internal | 7323.3, −4903.9 | 0 & 1 = 0 | external |
| | | 500 | 0 | −462.0, −933.7 | 1 & 1 = 1 | internal | 794.6, −540.1 | 0 & 1 = 0 | external |
| | $f_3$ | 0 | 0 | −4199.1, −15263 | 1 & 1 = 1 | internal | 11528, −7075.3 | 0 & 1 = 0 | external |
| | | 0 | 20 | −4090.0, −15177 | 1 & 1 = 1 | internal | 11428, −7046.7 | 0 & 1 = 0 | external |
| | | 500 | 0 | −367.0, −1345.7 | 1 & 1 = 1 | internal | 1005.7, −605.3 | 0 & 1 = 0 | external |
| | $f_4$ | 0 | 0 | −4195.1, 11514 | 1 & 0 = 0 | external | 11521, −7070.6 | 0 & 1 = 0 | external |
| | | 0 | 20 | −4138.5, 11495 | 1 & 0 = 0 | external | 11594, −7069.8 | 0 & 1 = 0 | external |
| | | 500 | 0 | −367.3, 1000.0 | 1 & 0 = 0 | external | 1003.9, −600.6 | 0 & 1 = 0 | external |
| ac fault | $f_6$ | 0 | 0 | 79.25, −63.09 | 1 & 0 = 0 | external | 31.59, −42.61 | 0 & 1 = 0 | external |

TABLE IV
PARAMETERS OF MMC STATIONS BUILT IN RTDS

| Parameter | Values |
|---|---|
| rated DC voltage (kV) | ±500 |
| rated AC voltage (kV) | 380 |
| rated capacity of $S_1$ and $S_2$ (MVA) | 1500, 3000 |
| inductance of one arm (mH) | 80 |
| SM capacitance of $S_1$ and $S_2$ ($\mu$F) | 15 000, 15 000 |
| number of SM in one arm | 220 |

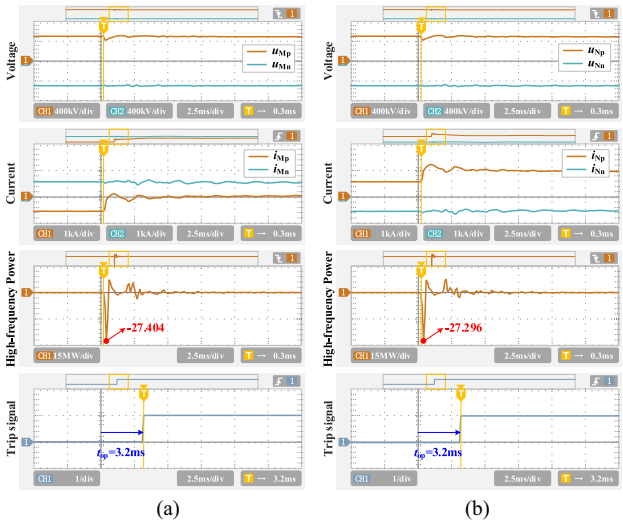


Fig. 9. Test results for an internal positive pole-to-ground fault at $f_2$ with a 500 Ω transition resistance (no boundary). (a) Signals at M. (b) Signals at N.

communication time delay). To further illustrate the sensitivity of the protection, Fig. 9 presents the measured voltage, current, high-frequency transient power, and trip signal after an internal high-resistance positive pole-to-ground fault (500 Ω, $f_2$). The results demonstrate that the high-frequency transient power maximum values calculated by both protections exhibit negative polarity. This allows for correctly identification of the fault as an internal fault, enabling a rapid trip response (both 3.2 ms).

Additionally, as shown in Table V, for faults occurring outside the protection zone ($f_4$ and $f_5$), the protection devices reliably do not operate. Fig. 10 illustrates the action results during an external metallic positive pole-to-ground fault ($f_4$) under boundary-less condition. The results clearly indicate that even under severe external faults, the protection devices can correctly distinguish the fault direction and segment, thereby exhibiting absolute selectivity.

## VI. COMPARISON OF THE PROPOSED METHOD WITH OTHER METHODS

This section compares the existing pilot protection methods with the proposed method. According to the working principle, typical pilot protections can be classified as current differential protection, transient power-based directional protection, directional overcurrent protection, travelling wave directional protection, boundary-based directional protection and protection based on other characteristics.

### A. Current Differential Protection

The sampled currents at the two ends of the line are in opposite directions when an external fault occurs, and the differential current is zero in theory. Differently, after an internal fault,

TABLE V
OPERATION RESULTS OF PROTECTION PROTOTYPE UNDER DIFFERENT FAULT CONDITIONS

| Boundary | Fault Type | Fault Location | Fault Resistance (Ω) | $p_{M\_hf}(k_{max})$ (MW) | $t_{op\_M}$ (ms) | $p_{N\_hf}(k_{max})$ (MW) | $t_{op\_N}$ (ms) |
|---|---|---|---|---|---|---|---|
| No boundary | pole-to-ground | $f_1$ | 0 | –1205.2 – –1064.4 | 3.0 – 3.9 | –553.5 – –499.7 | 2.3 – 3.2 |
| | | | 300 | –84.3 – –69.8 | 3.3 – 4.0 | –38.7 – –34.1 | 2.3 – 3.2 |
| | | | 500 | –40.2 – –39.6 | 3.0 – 4.2 | –14.5 – –14.2 | 2.8 – 3.2 |
| | | $f_2$ | 0 | –518.0 – –454.4 | 2.5 – 3.8 | –481.4 – –410.6 | 2.7 – 3.7 |
| | | | 300 | –62.7 – –53.5 | 2.9 – 4.0 | –62.3 – –52.4 | 2.5 – 3.9 |
| | | | 500 | –27.4 – –27.2 | 3.3– 3.6 | –27.5 – –27.1 | 3.1 – 3.5 |
| | | $f_3$ | 0 | –578.0 – –527.5 | 2.1 – 3.3 | –1252.6 – –1141.9 | 3.2 – 3.7 |
| | | | 300 | –39.9 – –31.5 | 2.5 – 3.4 | –83.6 – –68.4 | 3.4 – 4.0 |
| | | | 500 | –14.6 – –14.3 | 2.5 – 2.9 | –40.5 – –40.0 | 3.4 – 3.9 |
| | | $f_4$ | 0 | 798.0 – 810.9 | No Operation | –509.6 – –494.9 | No Operation |
| | | | 300 | 57.3 – 59.8 | No Operation | –33.2 – –31.7 | No Operation |
| | | | 500 | 25.5 – 25.8 | No Operation | –14.5 – –14.3 | No Operation |
| | | $f_5$ | 0 | 798.0 – 810.9 | No Operation | –509.6 – –494.9 | No Operation |
| | | | 300 | 57.3 – 59.8 | No Operation | –33.2 – –31.7 | No Operation |
| | | | 500 | 25.5 – 25.8 | No Operation | –15.5 – –14.3 | No Operation |
| | pole-to-pole | $f_1$ | 0 | –6633.8 – –6010.5 | 2.7 – 3.6 | –3178.5 – –2651.4 | 2.7 – 3.4 |
| | | | 300 | –943.9 – –814.8 | 3.0 – 4.6 | –453.9 – –444.4 | 2.4 – 3.9 |
| | | | 500 | –510.9 – –509.8 | 3.0 – 4.4 | –183.2 – –181.6 | 2.5 – 3.1 |
| | | $f_2$ | 0 | –3440.9 – –2885.6 | 2.7 – 4.0 | –3559.2 – –2837.6 | 3.1 – 4.1 |
| | | | 300 | –721.6 – –623.1 | 2.4 – 3.9 | –706.7 – –569.6 | 3.2 – 4.0 |
| | | | 500 | –343.0 – –342.2 | 3.2 – 3.8 | –343.2 – –341.7 | 2.4 – 3.3 |
| | | $f_3$ | 0 | –3325.3 – –3089.8 | 2.8 – 3.7 | –6934.1 – –6184.3 | 2.9 – 4.2 |
| | | | 300 | –721.6 – –623.1 | 3.0 – 3.5 | –976.0 – –828.0 | 3.8 – 4.5 |
| | | | 500 | –183.8 – –182.0 | 2.6 – 3.9 | –512.9 – –511.2 | 3.0 – 4.7 |
| | | $f_4$ | 0 | 4553.3 – 4581.7 | No Operation | –2726.7 – –2695.1 | No Operation |
| | | | 300 | 656.6 – 670.6 | No Operation | –364.3 – –359.4 | No Operation |
| | | | 500 | 326.2 – 328.0 | No Operation | –183.1 – –181.4 | No Operation |
| | | $f_5$ | 0 | –2813.7 – –2798.5 | No Operation | 4617.0 – 4639.2 | No Operation |
| | | | 300 | –369.0 – –360.4 | No Operation | 658.8 – 679.0 | No Operation |
| | | | 500 | –183.3 – –182.3 | No Operation | 327.5 – 328.6 | No Operation |
| With boundary $L_{dc}$ = 150 mH | pole-to-ground | $f_1$ | 0 | –131.8 – –117.2 | 2.7 – 3.8 | –318.2 – –271.7 | 2.2 – 3.4 |
| | | | 300 | –26.3 – –22.3 | 2.9 – 3.5 | –64.8 – –53.7 | 2.7 – 3.6 |
| | | | 500 | –12.9 – –12.8 | 3.6 – 4.4 | –31.6 – –31.3 | 2.5 – 2.9 |
| | | $f_2$ | 0 | –290.4 – –248.5 | 3.3 – 3.8 | –291.2 – –251.2 | 2.5 – 3.9 |
| | | | 300 | –28.6 – –26.9 | 2.7 – 3.6 | –29.5 – –27.1 | 3.0 – 3.6 |
| | | | 500 | –13.5 – –13.4 | 2.9 – 4.0 | –13.5 – –13.3 | 2.3 – 3.4 |
| | | $f_3$ | 0 | –317.3 – –278.7 | 2.7 – 3.2 | –131.3 – –118.3 | 3.0 – 3.8 |
| | | | 300 | –64.8 – –56.3 | 2.9 – 3.4 | –25.4 – –23.3 | 3.0 – 3.6 |
| | | | 500 | –31.6 – –31.4 | 3.0 – 3.5 | –13.0 – –12.8 | 2.6 – 4.1 |
| | | $f_4$ | 0 | 95.4 – 104.6 | No Operation | –67.5 – –61.3 | No Operation |
| | | | 300 | 11.4 – 12.9 | No Operation | –6.2 – –5.3 | No Operation |
| | | | 500 | 5.2 – 5.3 | No Operation | –2.4 – –2.3 | No Operation |
| | | $f_5$ | 0 | –68.5 – –63.2 | No Operation | 98.2 – 106.2 | No Operation |
| | | | 300 | –5.9 – –5.3 | No Operation | 11.3 – 12.1 | No Operation |
| | | | 500 | –2.4 – –2.3 | No Operation | 5.1 – 5.3 | No Operation |
| | pole-to-pole | $f_1$ | 0 | –755.0 – –718.7 | 3.2 – 3.9 | –1912.9 – –1724.3 | 2.3 – 3.4 |
| | | | 300 | –250.6 – –227.6 | 2.9 – 3.8 | –622.6 – –524.5 | 2.6 – 3.5 |
| | | | 500 | –142.8 – –142.4 | 3.4 – 4.0 | –346.1 – –345.6 | 2.6 – 3.5 |
| | | $f_2$ | 0 | –1940.7 – –1671.2 | 2.7 – 3.7 | –1926.3 – –1790.5 | 2.9 – 3.6 |
| | | | 300 | –394.5 – –375.2 | 2.5 – 3.9 | –402.9 – –360.4 | 3.4 – 3.9 |
| | | | 500 | –170.8 – –170.5 | 2.7 – 3.5 | –170.9 – –170.3 | 3.8 – 4.4 |
| | | $f_3$ | 0 | –1916.1 – –1606.1 | 2.3 – 3.0 | –769.7 – –718.0 | 3.6 – 4.0 |
| | | | 300 | –616.6 – –538.7 | 2.3 – 3.0 | –249.6 – –239.2 | 3.2 – 4.1 |
| | | | 500 | –348.4 – –347.0 | 2.8 – 3.8 | –143.7 – –143.2 | 3.1 – 4.6 |
| | | $f_4$ | 0 | 434.2 – 438.9 | No Operation | –286.6 – –282.7 | No Operation |
| | | | 300 | 115.7 – 124.7 | No Operation | –64.9 – –59.3 | No Operation |
| | | | 500 | 61.4 – 62.2 | No Operation | –30.2 – –29.8 | No Operation |
| | | $f_5$ | 0 | –280.7 – –276.2 | No Operation | 425.1 – 430.2 | No Operation |
| | | | 300 | –65.7 – –59.3 | No Operation | 115.4 – 121.5 | No Operation |
| | | | 500 | –30.2 – –30.0 | No Operation | 61.7 – 62.2 | No Operation |

the sampled currents at two ends are in the same direction, meaning the differential current is large. Current differential protection is based on this characteristic for fault identification. A major issue with traditional current differential protection in HVDC systems is the need to set a long-time delay to avoid the influence of distributed capacitance current. To address this, Tzelepis et al. [13] proposed to install multiple sensors along the line to partially compensate for the distributed capacitance current. However, this method leads to increased cost and heightened communication requirement. Gao et al. [14] and

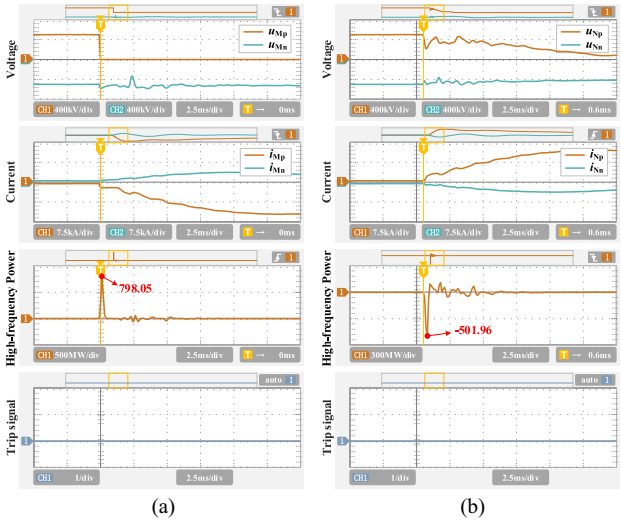


Fig. 10. Test results for an external positive pole-to-ground metallic fault at $f_4$ (no boundary). (a) Signals at M. (b) Signals at N.

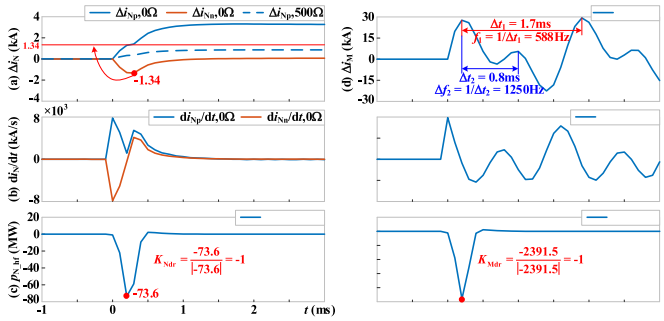


Fig. 11. Comparison of overcurrent directional protection and proposed method. (a) Current variation at N after positive pole-to-ground faults at $f_2$. (b) Current change rate at N after a positive pole-to-ground metallic fault at $f_2$. (c) High-frequency transient power at N after a positive pole-to-ground fault at $f_2$ with a 500 Ω transition resistance. (d) Current variation at M after a positive pole-to-ground metallic fault at $f_1$. (e) Current change rate at M after a positive pole-to-ground metallic fault at $f_1$. (f) High-frequency transient power at M after a positive pole-to-ground metallic fault at $f_1$.

Liu et al. [15] introduced the Bergeron distributed parameter model to accurately compensate for the distributed capacitance current. However, calculating the differential currents using the Bergeron model requires accurate acquisition of line wave impedance. In addition, although these methods improve the operation speed of current differential protection, they transmit the analogue current signals, which requires the signals to be strictly synchronized. In contrast, the method proposed in this paper only needs to transmit directional digital signals without data synchronization, which greatly reduces the complexity of engineering implementation.

### B. Transient Power-Based Directional Pilot Protection

Transient power is generally defined as the product of fault voltage and fault current. The direction of transient power flow differs after forward and backward faults, which can be utilized to design directional identification criteria. Zou et al. [27] characterized transient energy in terms of the integral of the transient power change, and constructed a directional criterion according to the polarity of transient energy. However, to avoid the energy fluctuation of the healthy pole caused by coupling during pole-to-ground faults, it is necessary to additionally set a threshold of the energy amplitude by simulation. Luo et al. [28] proposed a pilot protection utilizing the directional characteristics of reactive power. However, due to the frequent exchange of reactive power between inductive and capacitive components in the early stage of faults, a delay of several tens of milliseconds must be set, resulting in a slower operation speed. Dong et al. [29] developed a fault identification criterion based on the energy difference of transient power at both ends of the line. The threshold of this method is highly dependent on factors such as line length, transition resistance, and power losses of lines, making it challenging to be calculated. Additionally, the aforementioned methods primarily focus on analysis and simulation within the context of LCC-HVDC systems, leaving their adaptability in other scenarios to be explored further. In contrast, the method proposed in this paper does not require threshold value selection, and both theoretical and experimental results demonstrate its applicability across various HVDC transmission scenarios.

### C. Directional Overcurrent Protection

This section conducts a comparative simulation of the performance of directional overcurrent protection and proposed directional protection. When a positive pole-to-ground metallic fault occurs at $f_2$ in Fig. 1, $\Delta i_N$ and $di_N/dt$ measured at protection N are displayed in Fig. 11(a) and (b). The simulation results indicated that, due to the influence of inter-pole line coupling [30], fault current also appears at the negative pole line (healthy pole). To avoid the effects of induced current, the $\Delta i$ criterion must be set with a certain threshold value. From Fig. 11(a), it is evident that the threshold for the $\Delta i$ directional criterion should be at least greater than 1.34 kA. However, when the transition resistance is relatively high, the value of $\Delta i$ becomes small, approaching or even falling below the threshold, significantly reducing the operation sensitivity and speed of the $\Delta i$-based directional overcurrent criterion [31]. In Fig. 11(a), the blue dashed line represents the current change measured at protection N during a positive pole-to-ground fault with a transition resistance of 500 Ω. Within 3 ms after the fault, $\Delta i_{Np}$ remains below 1.34 kA, causing the directional overcurrent criterion to delay its operation or even refuse to operate. Furthermore, as shown in Fig. 11(b) the rate of change of induced current at the negative pole is comparable to that of fault current at the positive pole. When determining the fault direction according to $di/dt$, the healthy-pole directional criterion may operate by mistake.

The method proposed in this article utilizes decoupled line-mode voltage and current for calculation, thereby fundamentally avoiding the influence of line coupling. Additionally, the proposed algorithm identifies the fault direction by extracting the polarity of the maximum value of high-frequency transient power, eliminating the requirement for threshold setting. As shown in Fig. 11(c), even under high-resistance faults, the maximum polarity characteristics of the high-frequency transient power $p_{N\_hf}$ at N remain very pronounced (negative), allowing protection N to quickly identify the forward fault with high

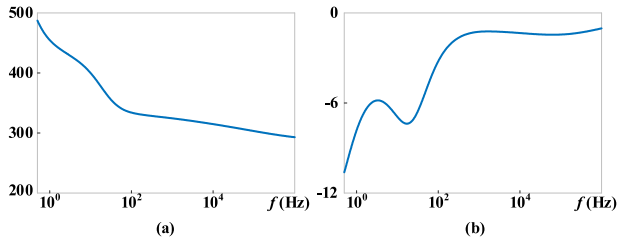


Fig. 12. Frequency characteristics of line wave impedance $Z_C$. (a) Magnitude of $Z_C$ under different frequencies. (b) Phase of $Z_C$ under different frequencies.

sensitivity. In fact, many scholars have researched and improved traditional directional overcurrent criteria. For example, papers [30], [32], and [33] enhanced the disturbance immunity of directional overcurrent protection by methods such as current integration. However, they still face the drawback of relying on extensive simulations to determine threshold values.

Moreover, in the system shown in Fig. 1, when a fault occurs near the LCC outlet ($f_1$), the dc filter will form a resonant circuit with the fault point, resulting in resonant currents flowing through the protection. As shown in Fig. 11(d) and (e), when a positive pole-to-ground metallic fault occurs at $f_1$, $\Delta i$ and d$i$/d$t$ measured by protection M exhibit alternating oscillations, with oscillation frequencies approaching the tuning frequencies (600 and 1200 Hz) of the dc filter, and the positive and negative peak values being relatively close. In this scenario, the directional overcurrent protection will struggle to quickly and reliably identify the fault direction. However, the proposed method, as discussed in Section III-B, avoids the influence of tuning frequencies by selecting appropriate frequency band ranges. Therefore, it can still reliably identify the fault direction under this condition [see Fig. 11(f)].

### D. Travelling Wave Directional Protection

After a backward fault, only forward TWs are present at the protection in the initial stage. Conversely, after a forward fault, both forward and backward TWs coexist. This observation allows for the design of direction criteria. Kong et al. [16] characterized the energy of TWs by the sum of the squares of the voltage TW ($u \pm Z_C \cdot i$) and constructed directional criteria based on the differences in TW energy between forward and backward faults. However, the TW directional protection is highly dependent on system parameters, specifically the line wave impedance. Despite the existence of established methods for calculating wave impedance, in protection devices, wave impedance needs to be set to a constant value. Given that line parameters exhibit frequency-dependent characteristics, the magnitude and phase of wave impedance continually changes with different frequencies, as illustrated in Fig. 12 (taking the line with physical parameters in Table II for instance). If the value of $Z_C$ selected in the protection algorithm is not optimal, significant discrepancies between the calculated TW and actual TW may arise, leading to reduced operation reliability of the protection [18]. To address this issue, Li et al. [18] extracted high-frequency transient TWs and utilized the constant amplitude characteristics of $Z_C$ in high-frequency range to mitigate the impact of parameter frequency-dependent characteristics. Li et al. [34] further concluded that as long as $Z_C$ is set to a value in the high-frequency range, the computed voltage TW would sufficiently reflect the actual TW. On this basis, a time-domain TW directional protection criterion was introduced that does not require the extraction of high-frequency signals, thus reducing implementation complexity.

Although substantial improvements have been made in TW directional protection, accurately obtaining the $Z_C$ value remains unavoidable. In scenarios where system parameters are difficult to obtain, such as in desert wastelands or deep oceans, the reliability of protection will be significantly diminished. Furthermore, He et al. [35] indicate that the natural frequency of fault signals in dc lines after a fault is closely related to factors such as fault distance and fault type. In other words, the frequency ranges where energy of electrical quantities is concentrated during faults vary under different conditions, leading to different wave impedances that should be used for calculating TWs for various faults. The TW calculated using a fixed wave impedance may deviate significantly from the actual TW. Additionally, the line wave impedance will also gradually change due to factors such as geographical environment, operational conditions, and aging. Therefore, even if the wave impedance is set to an appropriate value, the reliability and sensitivity of TW directional protection will diminish over time as the actual wave impedance changes with environmental conditions. In contrast, the method proposed in this paper only requires the acquisition of sampled voltage and current, making it independent of system parameters and thus applicable across a broader range of scenarios. In addition, the proposed algorithm only uses the polarity of the maximum value of transient power to identify the fault direction, eliminating the need for setting threshold values. This further alleviates the workload for field engineering personnel.

### E. Boundary-Based Directional Pilot Protection

In HVDC transmission projects, the dc side of LCC is typically equipped with dc filters and smoothing reactors, while dc side of VSC is usually equipped with current-limiting reactors. These components serve as natural boundaries for distinguishing forward and backward faults, leading to the development of various boundary-based directional protection schemes. Reference [36] proposed a blocking-type directional pilot criterion based on the ratio of high-frequency voltage amplitudes on both sides of the line filter and smoothing reactors. Li et al. [37] and Haleem and Rajapakse [38] proposed directional criteria using the polarity and rate of change of voltage across current-limiting reactors. Moreover, Yu et al. [39] introduced the mathematical concept of the matrix spectral radius to design a directional criterion with strong anti-interference capability. The advantage of the aforementioned boundary-based directional pilot protection is their independence from system parameters. However, they are not applicable in scenarios where boundary elements are missing. In contrast, the method proposed in this paper does not rely on system parameters or line boundaries, thereby offering enhanced applicability.

TABLE VI
COMPARISON OF DIFFERENT PILOT PROTECTION METHODS

| Principle | Refs. | Adaptation Scenarios | Communication Requirement | Boundary Dependence | Parameter Dependence | Threshold Setting | HIL Testing |
|---|---|---|---|---|---|---|---|
| Current differential protection | [13] | MT VSC-HVDC | Very high | independent | independent | Simulation | Yes |
| | [14] | PP LCC-HVDC | High | independent | dependent | Simulation | No |
| | [15] | MT LCC-VSC-VSC-HVDC | High | independent | dependent | Simulation | No |
| Transient power-based directional pilot protection | **Proposed** | **MT LCC-VSC-VSC-HVDC MT VSC-HVDC** | **Low** | **independent** | **independent** | **No need** | **Yes** |
| | [27] | PP LCC-HVDC | Low | Undiscussed | independent | Simulation | No |
| | [28] | PP LCC-HVDC | Low | Undiscussed | independent | No need | No |
| | [29] | PP LCC-HVDC | Low | Undiscussed | independent | Simulation | No |
| Directional overcurrent protection | [30] | PP LCC-HVDC | Low | independent | independent | Simulation | No |
| | [32] | PP VSC-HVDC | Low | independent | independent | Simulation | No |
| | [33] | MT VSC-HVDC | Low | independent | independent | Simulation | No |
| Travelling wave directional protection | [16] | PP LCC-HVDC | Low | independent | dependent | No need | Yes |
| | [18] | MT LCC-VSC-VSC-HVDC | Low | independent | dependent | Simple | No |
| | [34] | MT VSC-HVDC | Low | independent | dependent | Simple | No |
| Boundary-based directional pilot protection | [36] | PP LCC-HVDC | Low | dependent | independent | Simple | No |
| | [37] | PP LCC-HVDC | Low | dependent | independent | Simple | No |
| | [38] | MT VSC-HVDC | Low | dependent | independent | Simulation | No |
| | [39] | MT VSC-HVDC | Low | dependent | independent | Calculation | No |
| protection based on other characteristics | [40] | MT VSC-HVDC | Low | independent | independent | Simulation | No |
| | [23] | MT VSC-HVDC | Low | independent | independent | Calculation | No |
| | [41] | MT VSC-HVDC | Low | dependent | independent | No need | Yes |

### *F. Pilot Protection Based on Other Characteristics*

Waveform correlation, measurement impedance characteristics, and model features can also be utilized to construct directional criteria. Farshad [40] distinguished fault direction by assessing the cosine similarity between measured and reference signals. However, the reference signal must be obtained through simulation. He et al. [23] employed the ratio of high-frequency to low-frequency impedance magnitudes as the basis for directional discrimination, which does not rely on boundary and system parameters, yet necessitates the establishment of thresholds based on upper and lower limits of the impedance ratio. Zhang et al. [41] utilized the concept of pattern recognition, employing the Pearson correlation coefficient between voltage and current, as well as between voltage and the derivative of current, to identify forward and backward faults, without dependence on system parameters and without the need for setting. However, this method is solely applicable to MMC-HVDC systems with boundary elements; in the absence of boundaries, the model relationships analyzed will be disrupted, rendering the protection ineffective. In contrast, the method proposed in this paper possesses the distinct advantages of being independent of line boundaries, independent of system parameters, and free from setting requirements, making it suitable for a variety of HVDC transmission systems.

The protection proposed in this article, as well as aforementioned existing methods, are evaluated from six aspects, i.e., adaptation scenarios, communication requirement, boundary dependence, parameter dependence, threshold setting, and HIL experimental testing. The comparison results are summarized in Table VI. In the table, "MT" stands for multiterminal and "PP" stands for point-to-point. "Simple" refers to the case where threshold values need to be set solely based on reliability coefficients, without the need for simulation or calculation. For example, the threshold value in paper [18] can be set at $K_{\text{set}} = 2$.

From Table VI, current differential protection requires strict synchronization, which results in high communication demands and increases the complexity of engineering implementation. Some transient power-based directional pilot protection methods can achieve independence from system parameters and do not require threshold value setting, but a longer delay is needed. However, these methods are analyzed and validated only in the LCC-HVDC scenario with filter boundaries. Their adaptability in other scenarios, with different boundaries, or in the absence of boundaries remains unknown. Additionally, the threshold values of most methods still rely on simulations. The main drawback of directional overcurrent protection is that its overcurrent threshold must be determined through simulation. TW directional protections rely on accurate acquisition of the line wave impedance $Z_{\text{C}}$. Boundary-based protection is not suitable for scenarios where boundaries are absent. Additionally, most existing studies remain at the theoretical stage, lacking the development and testing of practical devices. In contrast, the method proposed in this paper is applicable to a variety of HVDC transmission scenarios and boundary conditions, does not rely on system parameters, is free from threshold setting, and does not require data synchronization. Moreover, the protection device is developed and successfully validated through HIL testing, demonstrating outstanding engineering practicality and reliability.

Finally, it is important to note that although the method proposed in this article exhibits notable advantages across various aspects listed in Table VI, it also has certain limitation. In a broad sense, the algorithm falls within the category of TW protection, and significant fault TW characteristics only exist in the initial stage after faults. The high-frequency transient power polarity characteristics also hold only in the initial TW stage after faults. If the proposed algorithm does not operate after the protection has been started, it is advisable to block this protection function, to exclude the influence of sporadic factors such as short-term

communication interruption or data transmission error. In such cases, it should be employed in conjunction with other long-time-scale protection methods (e.g., current differential protection). For instance, the traditional current differential protection may need to be blocked by the impact of line distributed capacitance within hundred milliseconds at the early stage of the fault. During this period, the method proposed in this paper can be utilized for rapid fault identification. After a delay of several hundred milliseconds, the current differential protection can be deblocked to identify the fault line (if the proposed protection does not operate at this stage). These two methods operate in the early stage and steady stage of the fault respectively, which can constitute a main and backup protection scheme to further enhance the reliability of dc line protection.

## VII. Conclusion

This study analyzed the characteristics of the transient power after faults in multiterminal HVDC systems under different line boundary conditions. Then, a novel directional pilot protection based on high-frequency transient power polarity was proposed. The conclusions are as follows.

1) The analysis of three typical boundary conditions, i.e., filter boundary, current-limiting reactor boundary, and no boundary, reveals that during forward faults, the polarity of the high-frequency power maximum measured by the protection is negative, regardless of the line boundary conditions. Conversely, after backward faults, the polarity of the high-frequency power maximum is positive.
2) According to the transient power polarity characteristic, a novel directional pilot protection is proposed. Compared to existing methods, the proposed method utilizes high-frequency power polarity features to identify fault segments without relying on line boundaries or system parameters, and does not require threshold setting. This significantly reduces the complexity of the engineering implementation, onsite operation, and maintenance, making it applicable to a wider range of scenarios.
3) A rapid directional pilot protection device for dc lines was developed based on the proposed principle. Extensive HIL experimental tests indicate that the developed prototype device exhibits absolute selectivity and high sensitivity under various boundary conditions of dc lines, while also demonstrating a high operating speed. This renders it suitable for various types of HVDC systems.

## References


[1] P. Verrax, A. Bertinato, M. Kieffer, and B. Raison, "Fast fault identification in bipolar HVDC grids: A fault parameter estimation approach," *IEEE Trans. Power Del.*, vol. 37, no. 1, pp. 258–267, Feb. 2022.

[2] Y. Zhang, Y. Li, J. Song, B. Li, and X. Chen, "A new protection scheme for HVDC transmission lines based on the specific frequency current of DC filter," *IEEE Trans. Power Del.*, vol. 34, no. 2, pp. 420–429, Apr. 2019.

[3] A. Prasai, J. Yim, D. Divan, A. Bendre, and S. Sul, "A new architecture for offshore wind farms," *IEEE Trans. Power Electron.*, vol. 23, no. 3, pp. 1198–1204, May 2008.

[4] B. Li, J. He, Y. Li, and B. Li, "A review of the protection for the multi-terminal VSC-HVDC grid," *Protection Control Modern Power Syst.*, vol. 4, no. 1, pp. 1–11, Jul. 2019.

[5] C. Zhang, G. Song, T. Wang, and X. Dong, "An improved non-unit traveling wave protection method with adaptive threshold value and its application in HVDC grids," *IEEE Trans. Power Del.*, vol. 35, no. 4, pp. 1800–1811, Aug. 2020.

[6] C. Zhang, G. Song, L. Yang, and X. Dong, "Non-unit travelling wave protection method for dc transmission line using waveform correlation calculation," *IET Gener. Transmiss. Distrib.*, vol. 14, no. 12, pp. 2263–2270, Jun. 2020.

[7] W. Xiang, S. Yang, G. P. Adam, H. Zhang, W. Zuo, and J. Wen, "DC fault protection algorithms of MMC-HVDC grids: Fault analysis, methodologies, experimental validations, and future trends," *IEEE Trans. Power Electron.*, vol. 36, no. 10, pp. 11245–11264, Oct. 2021.

[8] C. Zhang, G. Song, A. P. S. Meliopoulos, and X. Dong, "Setting-less nonunit protection method for DC line faults in VSC-MTdc systems," *IEEE Trans. Ind. Electron.*, vol. 69, no. 1, pp. 495–505, Jan. 2022.

[9] T. H. Nguyen, K. A. Hosani, M. S. E. Moursi, and F. Blaabjerg, "An overview of modular multilevel converters in HVDC transmission systems with STATCOM operation during pole-to-pole DC short circuits," *IEEE Trans. Power Electron.*, vol. 34, no. 5, pp. 4137–4160, May 2019.

[10] W. Leterme, P. D. Judge, J. Wylie, and T. C. Green, "Modeling of MMCs with controlled DC-side fault-blocking capability for DC protection studies," *IEEE Trans. Power Electron.*, vol. 35, no. 6, pp. 5753–5769, Jun. 2020.

[11] H. Li, M. Chen, B. Yang, F. Blaabjerg, and D. Xu, "Fast fault protection based on direction of fault current for the high-surety power-supply system," *IEEE Trans. Power Electron.*, vol. 34, no. 6, pp. 5787–5802, Jun. 2019.

[12] D. Mu, S. Lin, and X. Li, "Traveling wave characteristics based pilot protection scheme for hybrid cascaded HVDC transmission line," *J. Modern Power Syst. Clean Energy*, vol. 12, no. 3, pp. 971–980, May 2024.

[13] D. Tzelepis et al., "Single-ended differential protection in MTDC networks using optical sensors," *IEEE Trans. Power Del.*, vol. 32, no. 3, pp. 1605–1615, Jun. 2017.

[14] S. Gao, Q. Liu, and G. Song, "Current differential protection principle of HVDC transmission system," *IET Gener. Transmiss. Distrib.*, vol. 11, no. 5, pp. 1286–1292, Jan. 2017.

[15] H. Liu et al., "Ultra-fast current differential protection with high-sensitivity for HVDC transmission lines," *Int. J. Elect. Power Energy Syst.*, vol. 126, Mar. 2021, Art. no. 106580.

[16] F. Kong, Z. Hao, S. Zhang, and B. Zhang, "Development of a novel protection device for bipolar HVDC transmission lines," *IEEE Trans. Power Del.*, vol. 29, no. 5, pp. 2270–2278, Oct. 2014.

[17] X. Yu and L. Xiao, "A DC fault protection scheme for MMC-HVDC grids using new directional criterion," *IEEE Trans. Power Del.*, vol. 36, no. 1, pp. 441–451, Feb. 2021.

[18] B. Li et al., "An improved transient traveling-wave based direction criterion for multi-terminal HVDC grid," *IEEE Trans. Power Del.*, vol. 35, no. 5, pp. 2517–2529, Oct. 2020.

[19] Y. Li, J. Li, G. Wu, L. Xiong, K. Jia, and Z Xu, "DC fault analysis models of three converter topologies considering control effects," *IEEE Trans. Ind. Electron.*, vol. 67, no. 11, pp. 9480–9491, Nov. 2020.

[20] B. Li, Y. Li, J. He, and W. Wen, "A novel single-ended transient-voltage-based protection strategy for flexible DC grid," *IEEE Trans. Power Del.*, vol. 34, no. 5, pp. 1925–1937, Oct. 2019.

[21] F. Dai, Z. Zhou, and X. Wang, "Single-end protection scheme based on transient power waveshape for hybrid HVDC transmission lines," *J. Modern Power Syst. Clean Energy*, vol. 11, no. 5, pp. 1673–1686, Sep. 2023.

[22] H. Liu, J. Wen, S. Yu, J. Li, and T. Wang, "Research on design of DC filter systems of multiterminal DC Transmission systems," in *Proc. 4th Int. Conf. HVDC.*, 2020, pp. 46–51.

[23] J. He, Z. Xie, B. Li, Y. Li, H. Lyu, and Y. Sheng, "A novel directional pilot protection independent of line parameters and boundary elements for MMC-HVDC grid," *Int. J. Elect. Power Energy Syst.*, vol. 150, 2023, Art. no. 109094.

[24] A. R. Wood and J. Arrillaga, "The frequency dependent impedance of an HVDC converter," *IEEE Trans. Power Del.*, vol. 10, no. 3, pp. 1635–1641, Jul. 1995.

[25] K. Ji, H. Pang, J. Yang, and G. Tang, "DC side harmonic resonance analysis of MMC-HVDC considering wind farm integration," *IEEE Trans. Power Del.*, vol. 36, no. 1, pp. 254–266, Feb. 2021.

[26] L. Tang and B. T. Ooi, "Locating and isolating DC faults in multi-terminal DC systems," *IEEE Trans. Power Del.*, vol. 22, no. 3, pp. 1877–1884, Jul. 2007.

[27] G. Zou, Q. Huang, S. Song, B. Tong, and H. Gao, "Novel transient-energy-based directional pilot protection method for HVDC line," *Protection Control Modern Power Syst.*, vol. 2, no. 1, Apr. 2017, Art. no. 15.

[28] S. Luo, X. Dong, S. Shi, and B. Wang, "A directional protection scheme for HVDC transmission lines based on reactive energy," *IEEE Trans. Power Del.*, vol. 31, no. 1, pp. 559–567, Apr. 2016.
[29] Z. Dong, T. Ling, J. S. Thorp, and Y. Liang, "A transient harmonic current protection scheme for HVDC transmission line," *IEEE Trans. Power Del.*, vol. 27, no. 4, pp. 2278–2285, Oct. 2012.
[30] S. Gao, G. Song, Z. Ma, and X. Jin, "Novel pilot protection principle for high-voltage direct current transmission lines based on fault component current characteristics," *IET Gener. Transmiss. Distrib.*, vol. 9, no. 5, pp. 468–474, Apr. 2015.
[31] N. Geddada, Y. M. Yeap, and A. Ukil, "Experimental validation of fault identification in VSC-based DC grid system," *IEEE Trans. Ind. Electron.*, vol. 65, no. 6, pp. 4799–4809, Jun. 2018.
[32] G. Song, X. Chu, X. Cai, and S. Gao, "A novel pilot protection principle for VSC-HVDC cable lines based on fault component current," *Int. J. Elect. Power Energy Syst.*, vol. 53, pp. 426–433, Dec. 2013.
[33] S. Yang, W. Xiang, and J. Wen, "An improved DC fault protection scheme independent of boundary components for MMC based HVDC grids," *IEEE Trans. Power Del.*, vol. 36, no. 4, pp. 2520–2531, Aug. 2021.
[34] Y. Li, B. Li, J. He, H. Lyu, W. Wang, and Z. Xie, "Direction protection based on time-domain travelling wave for flexible MTDC grid," *CSEE J. Power Energy*, vol. 9, no. 4, pp. 1414–1424, Jul. 2023.
[35] Z. He, K. Liao, X. Li, S. Lin, J. Yang, and R. Mai, "Natural frequency-based line fault location in HVDC lines," *IEEE Trans. Power Del.*, vol. 29, no. 2, pp. 851–859, Apr. 2014.
[36] H. Shu, Y. Tian, S. Lei, G. Wang, X. Tian, and Y. Tang, "Accelerated backup protection for UHV long-distance hybrid cascaded DC transmission lines," *IEEE Trans. Ind. Electron.*, vol. 71, no. 8, pp. 9719–9726, Aug. 2024.
[37] Y. Li, Y. Zhang, J. Song, L. Zeng, and J. Zhang, "A novel pilot protection scheme for LCC-HVDC transmission lines based on smoothing-reactor voltage," *Elect. Power Syst. Res.*, vol. 168, pp. 261–268, Mar. 2019.
[38] N. M. Haleem and A. D. Rajapakse, "Application of new directional logic to improve DC side fault discrimination for high resistance faults in HVDC grids," *J. Modern Power Syst. Clean Energy*, vol. 5, no. 4, pp. 560–573, Jul. 2017.
[39] S. Yu, X. Wang, and C. Pang, "A pilot protection scheme of DC lines for MMC-HVDC grid using random matrix," *J. Modern. Power Syst. Clean Energy*, vol. 11, no. 3, pp. 950–966, May 2023.
[40] M. Farshad, "A pilot protection scheme for transmission lines of half-bridge MMC-HVDC grids using cosine distance criterion," *IEEE Trans. Power Del.*, vol. 36, no. 2, pp. 1089–1096, Apr. 2021.
[41] C. Zhang, B. Chen, A. Zhao, and G. Song, "Novel setting-less pilot protection for MMC HVDC grids," *Int. J. Elect. Power Energy Syst.*, vol. 164, Mar. 2025, Art. no. 110425.

**Jiawei He** (Member, IEEE) received the B.Sc., M.Sc., and Ph.D. degrees in electrical engineering from Tianjin University in 2014, 2017, and 2021, respectively.

He is currently an Associate Researcher Fellow with the School of Electrical and Information Engineering, Tianjin University. His research interests include protection and control of flexible dc grid, protection and control of power system with high proportion of renewable power generation.

**Mingyu Shao** received the B.Sc. degree in electrical engineering from Tianjin University, Tianjin, China, in 2023. He is currently working toward the M.Sc. degree in electrical engineering with the School of Electrical and Information Engineering, Tianjin University. His main research interests include protection and control of HVDC system.

**Bohao Zhou** received the B.Sc. degree in electrical engineering from Anhui University, Hefei, China, in 2018, the M.Sc. degree in electrical engineering from Xinjiang University, Xinjiang, China, in 2021, and the Ph.D. degree in electrical engineering from Tianjin University, Tianjin, China, in 2025.

He is currently an Assistant Researcher with the Energy Storage Industry-Education Integration Innovation Platform, Tianjin University. His research interests include protection and control of power systems with high penetration of power electronics and ultra-high voltage direct current (UHV dc) systems.

**Zhongrun Xie** received the B.Sc. and M.Sc. degrees from Shandong University, Jinan, China, in 2017 and 2020, respectively, and the Ph.D. degree from Tianjin University, Tianjin, China, in 2024, all in electrical engineering.

He is currently an Engineer with the Power Dispatch Control Center, Guizhou Power Grid Company Ltd. His current research interests include power system dispatching operation and control.

**Ye Li** received the B.Sc., M.Sc., and Ph.D. degrees from Tianjin University, Tianjin, China, in 2015, 2017, and 2021, respectively, all in electrical engineering.

She is currently serving as an Associate Professor with the Hebei University of Technology, Tianjin, China. Her research interests include protection and fault ride-through control of flexible dc grid, and protection and control of new power system with large-scale new energy access and so on.

**Jun Li** received the B.Sc. degree in electrical engineering and automation from the Tianjin University of Technology, Tianjin, China, in 2008. He is currently working toward the Ph.D. degree in electrical engineering with Tianjin University, Tianjin.

He works with the DC Technology Center of State Grid Corporation of China, Beijing, China, and is a Senior Engineer. His research interests include professional technical supervision and technical support for dc control and protection, operation, and maintenance.

**Bin Li** (Senior Member, IEEE) received the B.Sc., M.Sc., and Ph.D. degrees in electrical engineering from Tianjin University, Tianjin, China, in 1999, 2002, and 2005, respectively.

He was an academic visitor of the University of Manchester, Manchester, U.K., in 2006. And he worked in the design and application of protection relays in AREVA Company U.K. from 2008 to 2009. He is currently a Professor with the School of Electrical and Information Engineering, Tianjin University. His main research interests include the protection and control of power system.